

Very high cycle fatigue (VHCF) response of additively manufactured materials: A review

Original

Very high cycle fatigue (VHCF) response of additively manufactured materials: A review / Caivano, Riccardo; Tridello, Andrea; Chiandussi, Giorgio; Qian, Guian; Paolino, Davide; Berto, Filippo. - In: FATIGUE & FRACTURE OF ENGINEERING MATERIALS & STRUCTURES. - ISSN 8756-758X. - (2021). [10.1111/ffe.13567]

Availability:

This version is available at: 11583/2921732 since: 2021-09-07T10:44:29Z

Publisher:

Wiley Online Library

Published

DOI:10.1111/ffe.13567

Terms of use:

This article is made available under terms and conditions as specified in the corresponding bibliographic description in the repository

Publisher copyright

(Article begins on next page)

ORIGINAL ARTICLE

Very high cycle fatigue (VHCF) response of additively manufactured materials: A review

Riccardo Caivano¹  | Andrea Tridello¹  | Giorgio Chiandussi¹  |
Guian Qian²  | Davide Paolino¹  | Filippo Berto³ 

¹Department of Mechanical and Aerospace Engineering, Politecnico di Torino, Turin, Italy

²State Key Laboratory for Nonlinear Mechanics (LNM), Institute of Mechanics, Chinese Academy of Sciences, Beijing, China

³Department of Mechanical and Industrial Engineering, Norwegian University of Science and Technology (NTNU), Trondheim, Norway

Correspondence

Riccardo Caivano, Department of Mechanical and Aerospace Engineering, Politecnico di Torino, 10129, Turin, Italy.
Email: riccardo.caivano@polito.it

Abstract

Recently, the diffusion of components produced through additive manufacturing (AM) processes has significantly increased. Concurrently, to ensure the safe employment of AM components, the research has focused on the assessment of their fatigue response. In the present paper, a comprehensive literature review on the very high cycle fatigue (VHCF) response of materials produced through AM processes is provided. The experimental results on the VHCF response of Ti6Al4V, AlSi10Mg, AlSi7Mg, AlSi12, IN718, and 316L specimens produced through different AM processes are summarized. The main factors affecting the VHCF response of AM materials are finally compared and critically analyzed.

KEYWORDS

additive manufacturing (AM), aluminum alloy, IN718, Ti6Al4V, very high cycle fatigue (VHCF)

TERMINOLOGY LEGEND

AM Additive manufacturing

bal. Balance

BPH Base plate heating

DAS Dendrite arm spacing

EBM Electron beam melting

HCF High cycle fatigue

HIP Hot isostatically pressure

Horizontally built The angle between the building plate and specimen axis is 0°

ILB Improper layer bonding

LCF Low cycle fatigue

LOF Lack of fusion

μ-CT Micro-computed tomography

SEM Scanning electron microscope

SIF Stress intensity factor

SLM Selective laser melting

S-N Stress-life (number of cycles)

SR Stress relief

Vertically built The angle between the building plate and specimen axis is 90°

VHCF Very high cycle fatigue

wt % Weight percentage

1 | INTRODUCTION

In the last years, among the emerging processes to produce components employed in engineering applications, the additive manufacturing (AM) technology is one of the most employed, since it permits to produce parts with complex geometry, minimizing the manufacturing constraints. AM processes are widely employed for the

This is an open access article under the terms of the Creative Commons Attribution License, which permits use, distribution and reproduction in any medium, provided the original work is properly cited.

© 2021 The Authors. *Fatigue & Fracture of Engineering Materials & Structures* published by John Wiley & Sons Ltd.

production of components used in many different applications, like aerospace,^{1–5} motor race,⁶ and healthcare^{7,8} and are substituting traditional manufacturing processes in the production of heat exchangers,^{9,10} biomedical devices,¹¹ and structural brackets.^{12,13} For the production of metallic components, selective laser melting (SLM) and electron beam melting (EBM) are largely used. The research currently focuses on the optimization of these manufacturing processes in order to make them more efficient and effective in the production of components that can be safely used. For what concerns the use of AM components in structural applications, the focus is to guarantee the structural integrity of AM components in applications in which both static and fatigue loads are applied.^{14–17} In the literature, the quasi-static response of AM parts has been largely experimentally investigated.^{18–21} In addition, the response of AM specimens when fatigue loads are in the low cycle fatigue (LCF) and high cycle fatigue (HCF) regions has been also extensively investigated,^{22–25} focusing on the crack initiation and propagation mechanisms from manufacturing defects. Design methodologies have been also developed to prevent premature failures due to process-induced defects.¹⁶ On the other hand, the fatigue response of AM parts beyond 10^7 cycles, in the very high cycle fatigue (VHCF) regime,^{26–28} has been less extensively investigated in the literature, even if it is well known that the required fatigue of components is significantly larger than in the past and, for several applications, is even above 10^9 cycles. In Yamashita et al.²³ (“*Regarding the fatigue limit of Ni-based superalloy 718, a supplementary description may be necessary in terms of VHCF.*”) and in Shamsaei and Simsiriwong²⁹ (“*Due to the lack of VHCF studies for AM materials, there is a critical need to obtain the fatigue behaviour at gigacycles and the influences of design parameters, size/geometry, surface roughness, etc.*”), the need for the experimental assessment of the VHCF response of AM parts is clearly pointed out, in order to ensure their structural integrity and prevent failures due to low amplitude loads applied for a very high number of cycles. This would extend the knowledge on the fatigue response of AM components and would ensure their safe employment even in structural applications.

In the present paper, a comprehensive literature review on the VHCF response of parts produced through AM processes is provided. All the papers, published at present and focusing on the VHCF response of AM specimens, have been investigated. The main factors affecting the VHCF response of AM materials are compared and critically analyzed, highlighting the critical aspects that should be considered in the future research in this field.

For the sake of clarity, the paper has been organized by analyzing in each section the VHCF response of a

singular material. In Sections 1 and 2 the VHCF response of the AM aluminum alloys is reported. In Section 3 the VHCF response of Ti6Al4V, in Section 4 the VHCF response of Inconel 718, and finally, in Section 5 the VHCF response of 316L stainless steel are specifically described.

2 | VHCF RESPONSE OF AM MATERIAL

In the following sections, the fatigue response in the VHCF region of specimens produced through AM processes is analyzed in detail. Each investigated material has been considered separately. For each material, the experimental results obtained in the literature are at first analyzed and commented in a specific subsection (Section 2.1) and then compared in the subsequent subsection (Section 2.2).

The experimental data have been retrieved from tables, when available, or from the figures, by using the software *Engauge digitizer*. In the following, vertical specimens are those built with their axis perpendicular to the building platform (and parallel to the building direction), whereas horizontal specimens are the specimens produced with their axis parallel to the building platform (and perpendicular to the building direction). The defect at the origin of the fatigue failure will be called “critical defect.”

As will be highlighted in the following sections, the main fatigue failure cause of AM parts is the presence of defects. Indeed, AM materials are characterized by a non-negligible defect population. Minor fluctuations of the process parameters irreversibly lead to local imperfections, defects, and microstructural changes. These defects represent the preferred site for the nucleation and subsequent propagation of cracks, leading to the AM part collapse. The effect of size, location, and distribution of the defects is provided by the Murakami model,^{30,31} reported in Equation 1.

$$s = \frac{C_1 \cdot (HV + 120)}{(\sqrt{a_c})^{\frac{1}{6}}} \cdot \left(\frac{1 - R}{2} \right)^{0.226 + HV \cdot 10^{-4}} \quad (1)$$

where s is the VCHF strength at 10^9 cycles, C_1 is a constant parameter depending on the defect location, HV is the Vickers hardness, R is the stress ratio, and $\sqrt{a_c}$ is the equivalent critical defect size. This last term includes the effect of size, shape, and orientation of the critical defect. The location of the defect is considered by the constant term C_1 . If the defect is located superficially, this term is 40% smaller compared with internally located

one. Lastly, the distribution of the defects, that is, \sqrt{a} , inside the material is proved to follow the largest extreme value distribution (LEVD) as reported in Murakami.³¹

2.1 | VHCF response of AlSi12: Experimental results

In previous studies,^{32–36} the VHCF response of AlSi12 alloy processed by AM technologies is investigated. The specimens subjected to VHCF tests are manufactured by using an SLM 250 HL machine, by SLM Solution company, with a laser power of 400 W. A chessboard scanning strategy with 90° between the chess fields is used. The orientation field is rotated of 79° layer by layer to obtain isotropic properties in the final component. The fast-cooling rate of SLM additive process leads to a microstructure characterized by fine Si columnar dendrites along the scanning direction immersed in α -Al matrix. For a deeper analysis of the employed process parameters, scanning strategies, and resulting AlSi12 microstructure, the reader is referred to Siddique et al.³⁷ The AlSi12 powder contains (wt %) 11.62 Si, 0.72 Fe, 0.03 Cu, and bal. with a mean diameter of 33 μ m. Hourglass specimens with gage diameter of 3 mm are produced in vertical direction and thereafter machined before testing. Fully reversed tension compression VHCF tests up to 10⁹ cycles are experimentally assessed by using the ultrasonic fatigue testing system USF-2000 produced by Shimadzu at a loading frequency of 20 kHz.

In Siddique et al.³³ two different batches of specimens are compared, named B1 and B2. B1 is obtained without base plated heating (BPH), and B2 is obtained by heating the plate up to 200°C. Both undergo to a stress relief (SR) postprocess at 240°C followed by oven cooling. Figure 1 displays the S-N plot of the experimental data obtained in Rezvani Ghomi et al.⁷ The VHCF strength up to 10⁹ cycles for specimens belonging to B2 (with BPH) is 45% higher than that for specimens in B1, being 88.7 \pm 3.3 MPa for B2 and 60.5 \pm 4.7 MPa for B1, indicating a significant influence of the BPH. The scanning electron microscope (SEM) investigation of the fracture surfaces demonstrates that surface and internal defects are the main cause of crack initiation. In B1, crack initiation starts from surface as well as from subsurface pores; in B2, the crack initiation occurs mainly at the surface. The BPH permits to slightly reduce the residual porosity in the material and eliminate the largest process-induced pores thanks to the reduction in thermal gradients, enhancing the VHCF response.

In Siddique et al.³⁴ the influence of the BPH and the SR process on the fatigue life of AlSi12 is investigated. In particular, this study follows and confirms the results

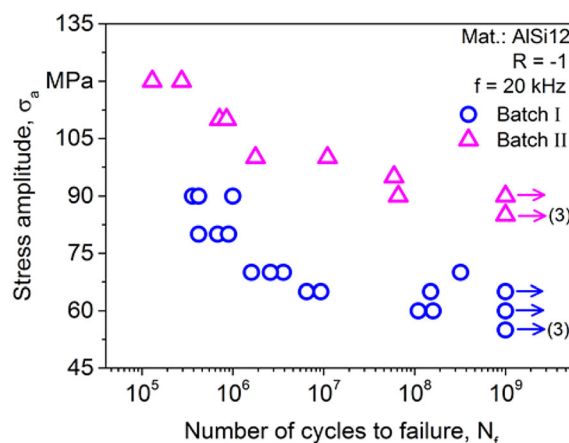


FIGURE 1 S-N plot of batch B1 (no base plate heating [BPH]) and batch B2 (with BPH) from Siddique et al.³³ [Colour figure can be viewed at wileyonlinelibrary.com]

TABLE 1 Parameters of the investigated batches in Siddique et al.³⁴

Batch	Base plate heating (BPH)	Stress relief (SR)
A	No	No
B	No	240°C
C	200°C	No
D	200°C	240°C

already obtained in Siddique et al.,³³ focusing mainly on the defect originating failures. Four batches, named A, B, C, and D are manufactured with the process parameters reported in Table 1. The microstructure is characterized by a very fine dendritic structure, with width range 0.3–0.6 μ m and Si precipitates. The porosity for all the samples results to be inferior to 0.3%: for batch A, 0.26%; for batch B, 0.38%; for batch C, 0.13%; and for batch D, 0.29%. Hence, the BPH decreases the overall porosity. On the other hand, the analysis on the defect size points out that the SR induces an expansion of the existing pores due to the internal pressure of trapped gas at high temperatures. Furthermore, the absence of BPH causes a nonuniform distribution of pores in terms of size and location. Overall, the BPH enhances the VHCF response due to inferior pores fraction and pore size. This effect is less evident in the HCF regime where even small pores, present in all the batches, become critical. It can be concluded that the VHCF strength is mainly controlled by microporosity, since only in a small number of failures the crack initiates from other material defects.

In Siddique et al.,³⁵ a comparison between the VHCF response of “pure” AlSi12 and “hybrid” AlZn4.5 Mg1 + AlSi12 specimens is carried out. The hybrid batch is obtained by using the AlZn4.5 Mg1 as solid base material

in the build chamber and by melting AlSi12 on the top of this base material as in the classical SLM process. The specimens are produced without heating the building platform and are subjected to the SR postprocess at 240°C followed by oven cooling at the end of the AM process. The hybrid specimens are built such that the interface between the two different materials lies in the middle of the longitudinal axis. The experimental tests are carried out up to 10^9 cycles: In particular, fatigue tests with a servo hydraulic testing machine (loading frequency of 20 Hz) are carried out up to 10^6 cycles, whereas ultrasonic fatigue tests are carried out to investigate to VHCF region. Figure 2 shows the S-N plot of the experimental data: Batch B refers to pure specimens, whereas Batch D to hybrid specimens. The VHCF strength up to 10^9 cycles of the hybrid material is equal to 80.7 MPa according to the S-N plot, considerably larger than that of the pure AlSi12 (about 59 MPa). The fatigue fracture in the hybrid specimens mainly occurs in the SLM part; however, the global fatigue limit is enhanced due to the progressive hardening which occurs in the material.

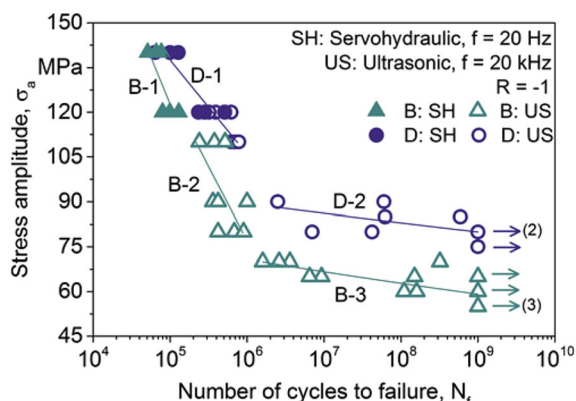


FIGURE 2 S-N plot of batch B (pure AlSi12) and batch D (hybrid AlZn4.5 Mg1 + AlSi12) from Siddique et al.³⁵ [Colour figure can be viewed at [wileyonlinelibrary.com](#)]

In Tenkamp et al.³² a comparison between the VHCF strength of die-cast alloy AlSi7Mg0.3 and additively manufactured AlSi12 is carried out. Die-cast (DC) samples are manufactured by gravity die-casting, including alloying procedure with AlTi5B1 and Sr. The melt is heated up to 730°C, and the steel mold is preheated to 450°C. Three batches are produced: DC1 as cast, DC2 with melt cleaning, and DC3 with melt cleaning and HIP process by Bodycote Densal™. All DC batches are afterwards subjected to a T6 process. AM AlSi12 specimens are produced including BPH. Two different batches are manufactured: batch AM1 including as-built (AB) specimens and batch AM2 including specimens subjected to the SR postprocess at 240°C in oven. Before testing, the gage diameter of all batches is ground and polished up to 1-μm diamond paste. The microstructure of the DC specimens shows a dendritic width about 2 orders of magnitude larger than that of the AM specimens. In addition, the pores in DC1 and DC2 are in average one order of magnitude bigger and less spherical than DC3, AM1, and AM2. Figure 3A shows the S-N plot of the DC batches, whereas Figure 3B shows the S-N plot of the AM batches. As for the DC specimens, the DC3 is characterized by the highest VHCF strength up to 10^9 cycles, approximately 83 MPa by graphical extrapolation, outperforming the other DC batches. For the AM specimens, the AM2 batch (SLM with BPH and SR) is characterized by the largest VHCF strength (approximately 88 MPa for the AM2 and 62 MPa for the AM1). The enhancement of the VHCF response of AM2 specimens is justified by the authors by considering that the SR process increases the sphericity of the internal pores, reducing the influence of internal micronotches. Moreover, the combination of BPH and SR in AM AlSi12 permits to obtain a VHCF strength larger than that of traditional die-cast AlSi7Mg0.3 alloy.

In Awd et al.³⁶ the influence of process parameters and postprocesses on the microstructure and VHCF response behavior of AlSi12 and AlSi10Mg alloy is investigated. Two different batches are compared, named A

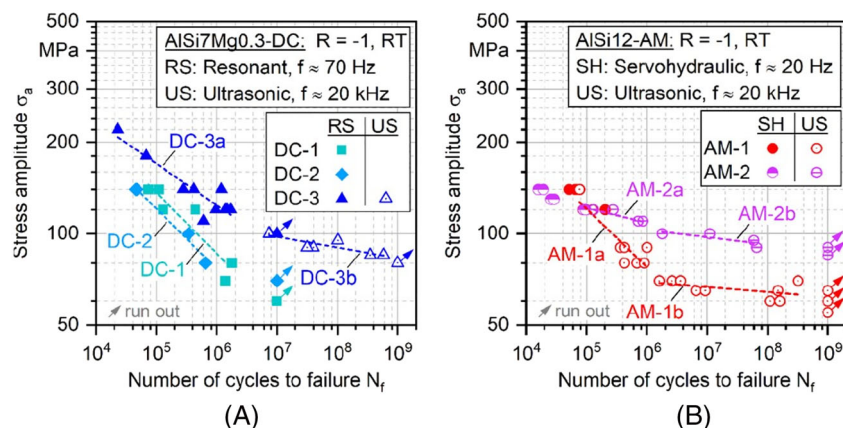


FIGURE 3 S-N plot of (A) batch DC (die-cast process) and (B) AM (1-no SR, 2-with SR) from Tenkamp et al.³² [Colour figure can be viewed at [wileyonlinelibrary.com](#)]

and B. A is obtained without BPH, and B is obtained by heating the plate up to 200°C. Both undergo to a SR post-process at 240°C followed by oven cooling. The process parameters are the same detailed at the beginning of this paragraph. Micro-computed tomography (micro-CT or μ -CT) analyses have been carried out to compare the porosity of specimens. The results obtained by the authors are shown in Figure 4A. As it can be noticed, BPH (batch B) reduces consistently the pore density in the specimen. Figure 4B shows the frequency of occurrence of pore diameters: In both the batches the mean value of the pore diameter is approximately 40 μm . However, the BPH remarkably decreases the pore density, according to Figure 4B.

This analysis confirms the experimental results found in previous research: The BPH significantly diminishes the microporosity and fosters the VHCF strength. The results on the AlSi10Mg alloy are analyzed in Section 2.

2.2 | VHCF strength of AlSi12: Discussion

In this section the experimental data on the VHCF response of AM AlSi12 alloy obtained in the literature are critically compared. The analysis of the fracture surfaces reveals that the VHCF response of AlSi12 alloy is driven by process-induced porosity in the material. The threshold stress level which separates the HCF from the VHCF regime is approximately 100 MPa. The influence of BPH and of SR treatment on the VHCF response is mainly investigated.

The BPH reduces the final porosity fraction in the material, increasing by about the 45% the VHCF strength, even if the mean pore diameter is left unaltered: Indeed, BPH permits to reduce the size of the largest pores. The BPH with the SR produces a reduction in the material hardness of about the 15% compared with AB samples. For more, in specimens produced without BPH, the scatter associated to the VHCF strength is larger due to a less uniform distribution of the pores, in terms of size and

location. An SR treatment increases the dimension of the pores due to the gas expansion in the heating process, but in contrast, it also enhances the VHCF strength of about 20% by increasing the sphericity of the pores and limiting internal micronotches due to irregular shapes. The VHCF response of hybrid material AlZn4.5 Mg1 + AlSi12 is 25% larger than that of pure AlSi12.

In conclusion, BPH positively affects the VHCF response, since it permits to reduce the porosity density and avoid the formation of very large pores. On the other hand, an SR treatment could have a positive influence on the VHCF response, since it enhances the defect sphericity, but it can also induce an increment of the pore size, which should be avoided in case of failures from defects. Compared with the traditional die-cast AlSi7Mg0.3 alloy, the additively manufactured AlSi12 outlines a 7% improved VHCF strength. Table 2 summarizes the experimental results on the VHCF response of AlSi12, reporting the main process parameters investigated in the literature.

2.3 | VHCF strength of AlSi12: Summary

For the AlSi12 specimens, the influence of the base plate heating (BPH) and of a SR heat treatment is mainly investigated:

- The BPH (200°C) reduces the final porosity and increases the VHCF strength.
- SR (240°C—2 h) treatment enhances the VHCF strength.
- The hybrid material AlZn4.5 Mg1 + AlSi12 presents an improved VHCF performance.

2.4 | VHCF strength of AlSi10Mg and AlSi7Mg: Experimental results

The effect of BPH on the VHCF response of AlSi10Mg specimens produced through SLM is experimentally

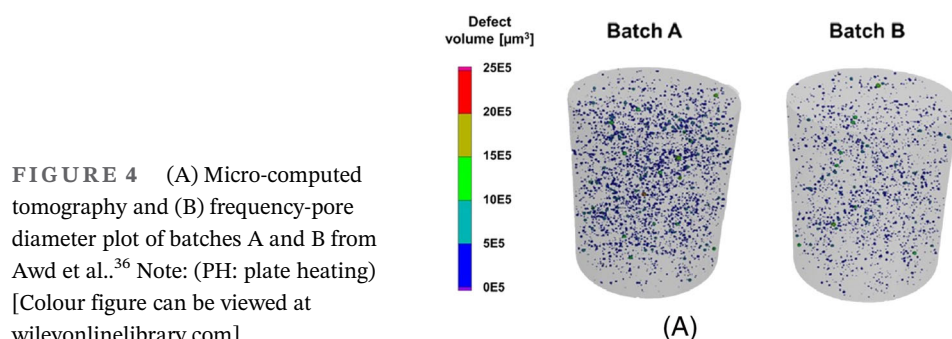


FIGURE 4 (A) Micro-computed tomography and (B) frequency-pore diameter plot of batches A and B from Awd et al.³⁶ Note: (PH: plate heating) [Colour figure can be viewed at wileyonlinelibrary.com]

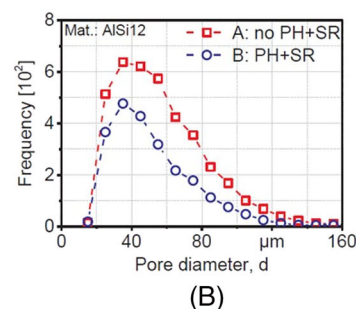


TABLE 2 VHCF strength of AM AlSi12 depending on process setup

Pure AlSi12 (SLM process and final machining)					
Specimen type	Building orientation	Base plate heating (BPH)	Stress relief (SR) and oven cooling	Runout	VHCF strength (MPa)
Hourglass ³³	Vertical	\	240°C	10 ⁹	60.5 ± 4.7
Hourglass ³³	Vertical	200°C	240°C	10 ⁹	88.7 ± 3.3
Hourglass ³⁵	Vertical	\	240°C	10 ⁹	59
Hourglass ³²	Vertical	200°C	\	10 ⁹	62
Hourglass ³²	Vertical	200°C	240°C	10 ⁹	88
Hybrid AlZn4.5 Mg1 + AlSi12 (SLM process and final machining)					
Hourglass ³⁵	Vertical	\	240°C	10 ⁹	80.7

Abbreviation: VHCF, very high cycle fatigue.

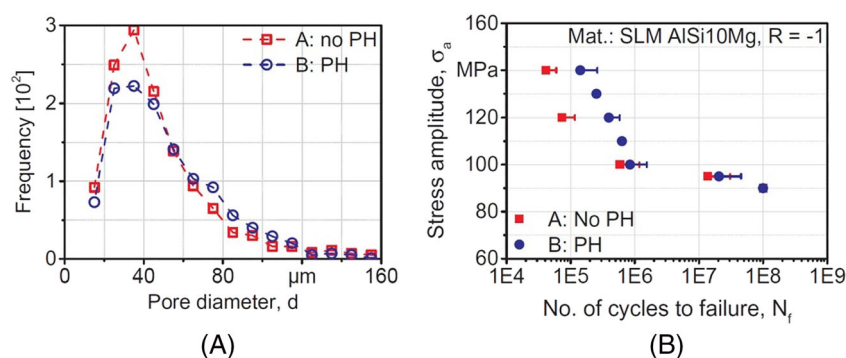


FIGURE 5 Experimental results in Awd et al.³⁸: (A) frequency of occurrence with respect to pore diameter; (B) fatigue life mean and standard deviation on a S-N plot. Note: (PH: plate heating) [Colour figure can be viewed at wileyonlinelibrary.com]

assessed in Awd et al.³⁸ A modified SLM 250 HL system with an external laser source with laser power of 1 kW is employed, and a two-step scanning strategy consisting of two contour scans followed by the core bidirectional scanning is employed to ensure high-quality parts and porosity less than 0.5%. Fully reversed tension-compression tests at 20 kHz up to 10⁸ cycles are carried out with a Shimadzu USF-2000A ultrasonic testing system on hourglass specimens built in vertical direction and thereafter machined to the final geometry. Two different batches are analyzed: Batch A is obtained without BPH and batch B is obtained by heating the plate up to 200°C. No SR postprocess is applied, in order to isolate the effect of the BPH. The microstructure of the specimens in both batches is characterized by an Al matrix with embedded network of equiaxed cellular Si boundaries parallel to the build platform and Si columnar dendrites along the building axis, with local coarsening along the melt pool track overlaps. However, the microstructure of the batch B (with BPH) presents a coarser morphology, a greater dispersion, and supersaturation of Si in the Al matrix, fewer Si semicoherent particles, and a larger number of Mg₂Si precipitates at the grain boundaries. The manufacturing defects have been

also analyzed: The average pore diameter is similar in both the batches (Figure 5A) even if the pores in batch B are characterized by a more spherical shape. Batch B shows an enhanced quasistatic, LCF and HCF strength due to the strengthening effect induced by these microstructure modifications. On the other hand, batches A and B show similar VHCF strength up to 10⁹ cycles, being about 90 MPa, according to the S-N plot in Figure 5B. Indeed, the VCHF response is found to be driven by the microporosity in both batches: More specifically, in batch A the crack initiation starts from a single critical defect, while in batch B multiple crack initiations occur. The BPH reduces the largest pore size but increases the pore number in the material. The authors conclude that the fatigue strength of platform heated specimens is higher in the VHCF regime due to the influence of defect morphology and microstructure. However, the increment is not significant due to the large scatter of the experimental data. The main effect of BPH is the reduction of the scatter associated to the VHCF results.

Awd, in,³⁶ further analyzes the experimental results in a previous study,³⁸ in particular by considering the defect density and distribution. The μ -CT of the samples obtained in Singh and Ramakrishna¹¹ is reported in

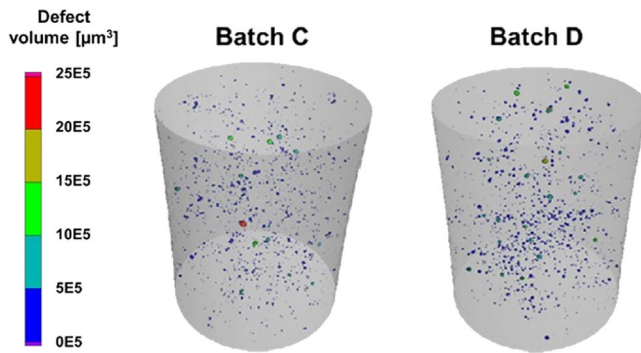


FIGURE 6 Micro-computed tomography of batches C and D from Awd et al.³⁶ [Colour figure can be viewed at wileyonlinelibrary.com]

Figure 6. As it can be noticed, the μ -CT proves that the BPH has not a remarkable effect on the final porosity. This confirms why BPH does not affect the VHCF response.³⁸ Spherical gas porosities located sub-superficially result to be the most critical defect for the VHCF response.

In previous studies,^{39–44} fully reversed ultrasonic tension–compression VHCF tests up to 10^9 cycles on AlSi10Mg Gaussian specimens are carried out. The tested Gaussian specimens are characterized by a risk volume³¹ (above 2000 mm³) significantly larger than that of hour-glass specimens commonly tested in the literature, permitting to take into account the dependency between the defect size distribution and the risk volume. The SLM specimens are produced with an SLM Solutions system (model 500 HL with four continuous fiber lasers with power of 400 W). Standard industrial process parameters by the SLM system are selected to manufacture high-quality parts (including BPH at 150°C). Spherical gas atomized powder with a mean diameter of 45 μ m is used. The manufactured specimens are manually polished to reduce the roughness of the surface and remove a layer of surface material thinner than that removed with other processes (e.g., machining). The microstructure is characterized by columnar solidification structure following the shape of localized melting pools. A complete and detailed description of the AlSi10Mg microstructure by SLM process is provided in previous studies.^{45,46}

In Tridello et al.,³⁹ the VHCF strength of horizontally AB AlSi10Mg samples is investigated. Figure 7 shows the S-N plot of the experimental dataset: On the abscissa axis the stress amplitude close to the defect location, s_{local} , is reported. The smallest s_{local} at runout is found at 68 MPa. Surface and subsurface defects are found to be responsible for the crack initiation in all the experimental failures. The reasons for this behavior are mainly three. First, defects close to the surface are known to be more

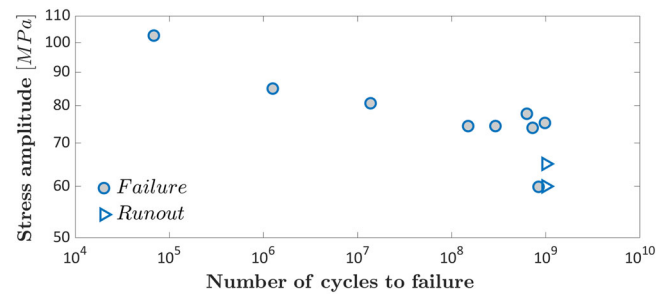


FIGURE 7 S-N plot of the experimental data obtained considering the local stress close to the defect size s_{local} from Tridello et al.³⁹ [Colour figure can be viewed at wileyonlinelibrary.com]

detrimental than internal ones (i.e., the stress intensity factor [SIF] of surface defects is approximately 32% larger than the SIF of internal defects³¹). Second, residual stresses tend to be larger close to the surface due to higher thermal gradients. Third, the horizontally built specimens need to be supported in the overhang portion of the surface. The afterwards support removal creates many superficial defects which are detrimental for the fatigue response. The critical defect type is also analyzed, being in the 67% of the cases cluster of pores, in the 22% surface defects, and in the 11% lack of fusion (LOF) defects. According to these analyses, the authors conclude that the removal of the most external layer of material, for example, through a machining process, would eliminate the most defect-dense zone and would likely enhance the VHCF strength.

In Tridello et al.,⁴⁰ the influence of SR heat treatments on the VHCF response of AlSi10Mg specimens is investigated. Two SR heat treatments characterized by two different heating temperatures are considered. The first one, HT-320, is suggested by the AM system manufacturer and involves annealing process for 2 h at 320°C followed by oven cooling. The second one, HT-244, is optimized by the authors and involves annealing at 244°C for 2 h and then oven cooling. The investigated SR treatments are applied to specimens built in horizontal direction, and their effect on the VHCF response is investigated by considering the experimental results on AB specimens in Tridello et al.³⁹ Microstructural analyses are at first carried out with the SEM; in particular, it is found that a heating temperature of 320°C modifies the final microstructure. Indeed, the continuous network of eutectic Si, typical of AB specimens, is modified, and the final microstructure is characterized by embedded spherical Si particles within the Al matrix. The microstructural change induces a significant reduction of the Vickers hardness, about 42%, and of the tensile strength (about

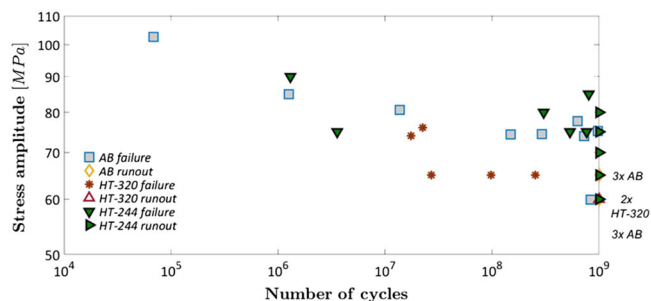


FIGURE 8 Stress-life (S-N) plot of the experimental data obtained considering s_{local} from Tridello et al.⁴¹ [Colour figure can be viewed at wileyonlinelibrary.com]

50%), whereas the elongation to failure significantly increases (2.4 times). On the contrary, the HT-244 post-process induces a coarsening of the Si network, but it does not modify its morphology. Consequently, the reduction of the HV hardness is limited to 13% with respect to AB specimens and the tensile properties are close to that of AB specimens. The S-N plot of experimental data with respect to stress amplitude close to the defect location s_{local} is shown in Figure 8.

The defect originating the fatigue failures is analyzed. As for AB specimens, surface and subsurface cluster and single pores are the most critical defects in HT-320 specimens. In HT-244 the most critical defects are LOF, differently from AB and HT-320. The graphically extrapolated VHCF strength at 10^9 cycles for AB, HT-320, and HT-244 is 68, 61, and 76 MPa, respectively. The VHCF response of HT-244 specimens is improved due to the minimization of the residual stresses: On the other hand, the microstructural changes and the consequent Vickers hardness reduction in HT-320 significantly affect the VHCF response, even if the residual stresses are minimized.

In Paolino et al.⁴² the VHCF response of AlSi10Mg AB samples built in vertical direction is investigated. As for horizontally built specimens,¹⁴ the microstructure is characterized by a continuous eutectic Si network embedded in a supersaturated Al matrix, elongated in the building direction. The S-N plot of experimental data with respect s_{local} is shown in Figure 9. The VHCF response shows a large scatter, mainly associated to the large dispersion associated to the critical defect size. The VHCF strength at 10^9 cycles is graphically estimated as approximately 63 MPa. The SEM inspection of fracture surface reveals that two different types of subsurface defects initiate the crack: LOF defects and defect due to improper layer bonding (ILB defects). Most of the critical defects are found to be smaller than 200 μm , but three significantly larger defects, with size larger 200 μm , are also found. This contributes to the large experimental

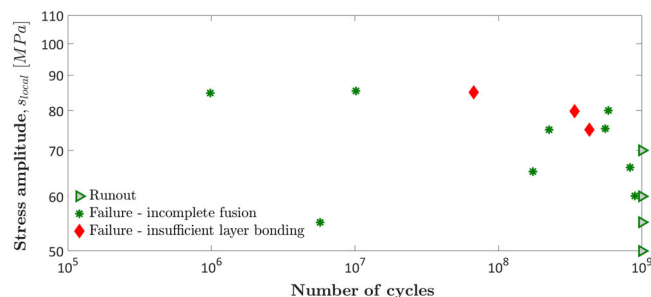


FIGURE 9 Stress-life (S-N) plot of the experimental data obtained considering s_{local} from in Paolino⁴² [Colour figure can be viewed at wileyonlinelibrary.com]

scatter: For example, the specimens containing the largest defect (equivalent size of 286 μm) failed at a number of cycles smaller than 10^7 for a stress amplitude of 58 MPa. On the other hand, a specimen tested at the same stress amplitude did not fail at 10^9 cycles.

In Tridello et al.⁴³ a critical analysis on the effect of microstructure, residual stress, and building orientation on VHCF response of AlSi10Mg is carried out by analyzing the experimental data in previous studies^{39–42} with models available in the literature and statistical models proposed by the authors. In particular, the VHCF strengths at 10^9 cycles for the defect with median size in each group are at first compared (being s_{AB-H} , s_{HT-320} and s_{HT-244} the VHCF strength at 10^9 cycles for AB, HT320 and HT244 specimens, respectively) according to a statistical procedure reported on the paper. The ratios s_{AB-H}/s_{HT-320} , s_{HT-244}/s_{HT-320} and s_{HT-244}/s_{AB-H} and the corresponding confidence intervals are computed. This analysis confirms that the difference between s_{HT-244} and s_{HT-320} is statistically significant, proving that the microstructure plays a significant role and significantly affects the VHCF response (i.e., in both specimens the residual stresses are minimized and the difference is mainly due to the microstructure). On the other hand, no statistical difference between s_{AB-H} and s_{HT-320} and between s_{AB-H} and s_{HT-244} is found, even if the median s_{HT-244} is found to be the largest. By equalling the ratio s_{HT-244}/s_{AB-H} computed with Equation 1 with the same ratio computed by considering the median VHCF strength at 10^9 cycles, the residual stresses in AB specimens can be computed. Table 3 summarizes the main experimental data employed in the model and the estimated residual stresses for AB specimens.

According to Table 3, residual stresses in AB are found to be close to 100 MPa, in agreement with literature results in Colombo et al.⁴⁷ where the maximum principal residual stresses are experimentally assessed. These analyses justify the experimental results: Indeed, no statistical difference is found between s_{AB-H} ,

TABLE 3 Parameters for Murakami model in Tridello et al.⁴³ and estimated residual stresses in AB specimens

Batch (from Tridello et al. ⁴¹)	Critical defect size (mean) $\sqrt{a_c}$ (μm)	HV hardness	Residual stress (estimated) (MPa)	Stress ratio (estimated)	VCHF strength s_{10^9} (MPa)
AB	167	132	About 100	About 0.2	68
HT-320	88	76	0	−1	61
HT-244	183	115	0	−1	76

Abbreviation: HV, Vickers hardness; VCHF, very high cycle fatigue.

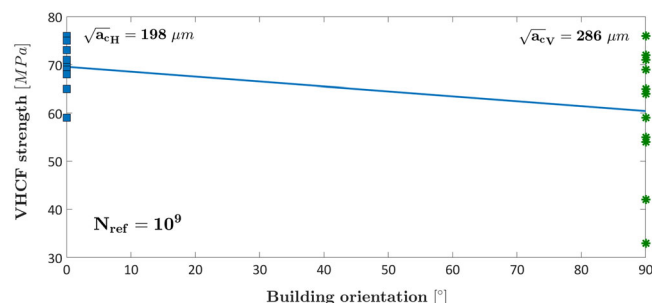


FIGURE 10 VCHF strength at 10^9 cycles for as-built specimens with respect to the building orientation: Experimental data and linear regression from Tridello et al.⁴³ [Colour figure can be viewed at wileyonlinelibrary.com]

s_{HT-320} , since the reduction of the Vickers hardness counterbalances the larger median defect and the presence of residual stresses in AB specimens. On the other hand, the larger median defect in HT-244 specimens is balanced by the high residual stresses in AB specimens: For this reason, the median VCHF strengths at 10^9 cycles in AB and HT-244 do not significantly differ. A similar analysis is carried out by the authors by comparing the VCHF strengths at 10^9 cycles for the largest defect found experimentally ($\sqrt{a_c}$ equal to $365 \mu\text{m}$), proving that there is an interaction between defect size and residual stresses and that the detrimental effect of residual stresses increases with the defect size.

The effect of the building orientation is also investigated in Tridello et al.⁴³ Figure 10 depicts the VCHF strengths of horizontal AB specimens (AB-H from Tridello et al.³⁹) and vertical AB specimens (AB-V from Paolino et al.⁴²) at 10^9 cycles with respect to the building angle (0° corresponds to the horizontal building orientation, whereas 90° corresponds to the vertical building orientation). The VCHF strength at 10^9 cycles is computed by considering the largest defect in AB-H and in AB-V. As shown in Figure 10, the VCHF strength is smaller for AB-V specimens, characterized by more dispersed experimental failures due to a large defect size range. The VCHF strength decrement with respect to the building angle is properly modeled with a linear interpolation.

Note: ($\sqrt{a_{cH}}$: largest critical defect size horizontal specimens, $\sqrt{a_{cV}}$: largest critical defect size vertical specimens, N_{ref} reference number of cycles)

In Tridello et al.⁴⁴ the effect of the specimen volume (size-effect) on the VCHF response of AlSi10Mg is investigated. The experimental results obtained by testing hourglass specimens, with a risk volume of 250 mm^3 , and Gaussian specimens, with a significantly larger risk volume of $2,330 \text{ mm}^3$, are analyzed. Hourglass and Gaussian specimens are manufactured in horizontal and vertical direction to assess the influence of the building orientation on size-effect. In the paper, the specimen type is identified by two capital letters: The first letter refers to the specimen type (H for the Hourglass and G for the Gaussian) and the second letter refers to the building orientation (H for the horizontally built specimens and V for the vertically built specimens). Figure 11A shows the S-N plot of the experimental data, whereas Figure 11B shows the estimated VCHF strengths at 10^9 cycles. The graphically estimated mean VCHF strengths at 10^9 cycles can be considered approximately as $97 \pm 10 \text{ MPa}$ for HH, $68 \pm 6.2 \text{ MPa}$ for GH, $68 \pm 13 \text{ MPa}$ for HV, and $55 \pm 16 \text{ MPa}$ for GV. As already reported in Paolino et al.,⁴² the vertical building direction induces larger scatter and smaller VCHF strength. Similarly, the VCHF strength of Gaussian specimens is smaller than that of hourglass specimens due to size-effects. Considering the horizontal batches, all the critical defects are superficial pores located in the support removal zones. Indeed, this region is characterized by a local smaller Vickers hardness and a larger pore density regardless of the sample geometry. Therefore, in the horizontal specimens, the size-effect is mainly related to the pore size, with the largest critical defect in Gaussian specimens 1.6 times larger than the largest critical defect in hourglass specimens. For the vertical specimens, the critical defects in the hourglass specimens are mainly superficial pores. On the other hand, larger LOF and ILB critical defects are found in Gaussian specimens. Therefore, size-effects not only affect the pore size but also the pore type. Experimental results confirmed that size-effects strongly affect the VCHF response, regardless of the building orientation and must be

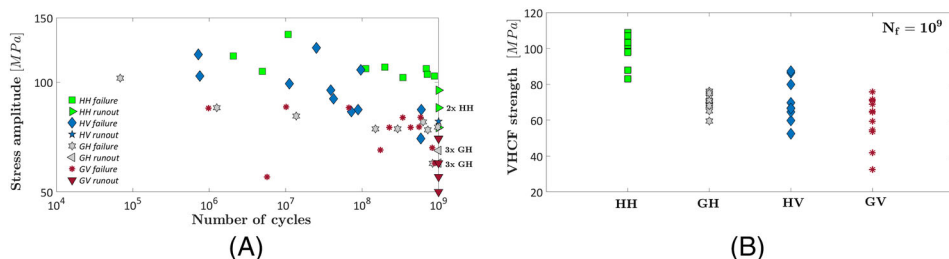


FIGURE 11 (A) Stress-life (S-N) plot of the experimental data obtained considering s_{local} and (B) estimated VHCF strength at 10^9 cycles from Tridello et al.⁴⁴ [Colour figure can be viewed at wileyonlinelibrary.com]

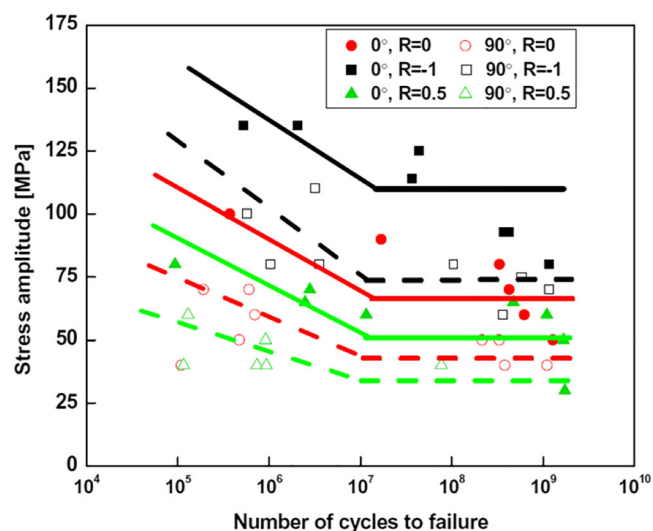


FIGURE 12 S-N plot of batches A and B under different mean stress from Qian et al.⁴⁸ [Colour figure can be viewed at wileyonlinelibrary.com]

carefully taken into account when the AM parts have to be designed.

In Qian et al.⁴⁸ the influence of building orientation and mean stress on the VHCF response of AlSi10Mg alloy specimens manufactured by SLM process is investigated. Hourglass specimens with gage diameter of 3.5 mm are manufactured with an SLM machine with a laser power of 370 W and with a preheating temperature of 35°C. Alloy powder with a mean diameter of 50 μm containing (wt %) 9.75 Si, 0.22 Mg, 0.01 Cu, 0.01 Cr, 0.01 Ni, 0.092 Fe, 0.01 Mn, 0.01 V, 0.01 Zn, 0.011 Ti, and bal. is used. The average surface roughness is 2.526 μm . The VHCF tests are carried out up to 10^9 cycles with a Lasur GF20-TC ultrasonic testing system (loading frequency of 20 kHz) integrated in a tensile machine, thus allowing to vary the mean stress. The effect of the building orientation is also investigated, by testing specimens produced in vertical and horizontal direction. The microstructure, in agreement with previous research, shows a fine Si network embedded in Al matrix in the plane parallel to the building plate, whereas a dendritic elongated structure perpendicularly to the building plate. Horizontal and

vertical specimens are tested at stress ratios, R , equal to -1 , 0 and 0.5 . The experimental results are reported in the S-N plot in Figure 12, which shows that horizontally built specimens are characterized by a better VHCF response for the same stress ratio. As already found in Paolino et al.,⁴² the vertically built samples are characterized by a lower VHCF strength mainly due to the presence of larger defects. In addition to the increased defect size, in vertical built specimens, the crack propagation occurs in the same layer, facing fewer obstacles, and it is fostered by possible existing discontinuities. The effect of the applied mean stress is clear, with the VHCF strength decreasing with the stress ratio. The critical defects are superficial, subsuperficial, and internal LOF; internal pores; unspecified defects from the rough surface; and tearing defects. The graphically estimated mean VHCF strengths at 10^9 cycles for horizontal specimens and R equal to -1 , 0 and 0.5 are 110, 66, and 51 MPa, respectively. For batch B the counterpart values are 74, 43, and 34 MPa.

In Jian et al.⁴⁹ the effect of different powder sizes on the VHCF response of AlSi10Mg alloy manufactured by SLM process is investigated. Hourglass specimens with gage diameter of 3.5 mm are manufactured with an SLM machine with a laser power of 370 W and with a preheating temperature of 35°C. The chemical composition of the powder is the same as in Qian et al.⁴⁸ The specimens are machined and polished to the final geometry without heat treatment. The VHCF tests are carried out with an ultrasonic testing system at 20 kHz up to 10^9 cycles. The specimens are produced by using a powder with mean size 20 μm (batch A) and a powder with mean size of 50 μm (batch B). The tests are carried out at different stress ratios (-1 , 0 , and 0.5). As for the microstructure, the results are in line with the previously described SLM AlSi10Mg samples, the morphology of the melt pool shows a fine grain area with smaller size grains and a coarser grain area at the boundary. The overlapping of the laser scan leaves a heat-affected zone with sparse grain distribution. Figure 13 shows the S-N plot of the experimental data. Two different conclusions are drawn by the authors: First, the increase of the stress ratio diminishes the VHCF strength as already found in

Qian et al.⁴⁸; second, the powder size strongly influences the VHCF response. The specimens produced with a smaller powder size are characterized by higher roughness, smaller hardness, and the critical defects are larger. The main reasons are the worse powder fluidity and the larger powder surface area that fosters gas inclusion. In batch A the critical defects are mostly subsuperficial and internal unmelt-powder. The largest defect size in batch A is almost double than the largest in batch B. The graphically estimated mean value of VHCF strength at 10^9 cycles and R equal to -1 for batch A is approximately 87 MPa, whereas it is 99 MPa for batch B.

In Lesperance et al.⁵⁰ the VHCF response of machined and heat-treated SLM AlSi10Mg and AlSi7Mg alloys is investigated. Cylindrical specimens are manufactured vertically with an SLM machine (EOS M290) with a laser power of 370 W and with a preheating

temperature of 180°C , following ISO 4497 standards. AlSi10Mg and AlSi7Mg alloy powders with diameter smaller than $63\ \mu\text{m}$ containing mainly (wt %) 9.0–11.0 Si, 0.2–0.45 Mg, and 6.7–7.3 Si, 0.5–0.6 Mg are used, respectively. The AM cylindrical specimens are subjected to a T6 heat treatment, namely, exposure at 535°C for 2 h followed by water quenching and aging at 170°C for 6 h. Finally, the specimens are machined to the final dog-bone (gauge diameter 4 mm) geometry for fatigue testing. An ultrasonic fatigue testing machine developed in-house by the authors is used with a frequency of 20 kHz. More details about this VHCF testing system is provided in Ilie et al.⁵¹ Figure 14A shows the S-N plot of the AlSi10Mg experimental data compared with literature heated-treated AlSi10Mg data. At 10^9 cycles, the VHCF strength is graphically estimated to be around 94 MPa. The authors highlight the difficulties in comparing experimental data from different experimental setups and claim that the effect of heat treatment is crucial, and it needs further investigations for practical applications. Figure 14B shows the S-N plot of the AlSi7Mg experimental data compared with literature cast AlSi7Mg data.

The results show a reasonable agreement, and the VHCF strength up to 10^9 cycles is graphically estimated to be approximately 65 MPa. Compared with the AlSi10Mg batch, the VHCF strength is about 30% smaller, which means that the AlSi7Mg alloy has a worse VHCF response under these conditions.

2.5 | VHCF strength of AlSi10Mg and AlSi7Mg: Discussion

Three research groups have focused their experimental activity on the assessment of the VHCF response of AlSi10Mg specimens. The main objectives are the

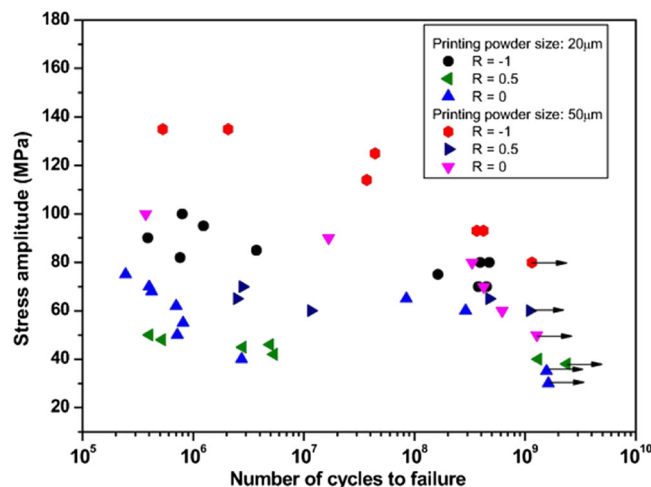


FIGURE 13 S-N plot of batches A and B under different mean stress from Jain et al.⁴⁹ [Colour figure can be viewed at wileyonlinelibrary.com]

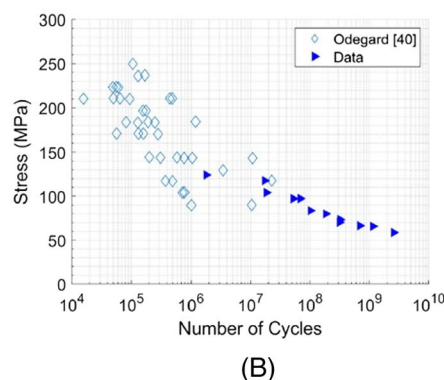
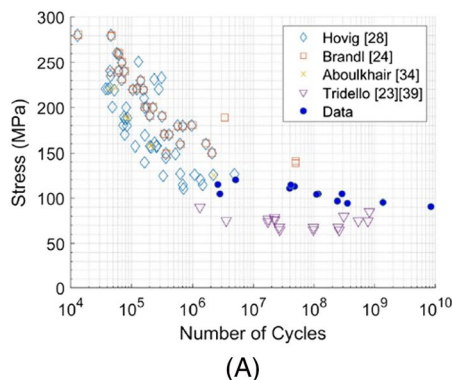


FIGURE 14 S-N plot of (A) AlSi10Mg batch compared with literature AlSi10Mg heat-treated data and (B) AlSi7Mg batch compared with literature cast AlSi7Mg data from Lesperance et al.⁵⁰ Note: The legend in the plot link to literature VHCF data which are in this paper renumbered as Tridello et al.⁴³ (Yamashita et al.²³ in the plot) Tridello et al.⁴⁰ (Tridello et al.³⁹ in the plot). For the other references about HCF data, the reader is referred to Lesperance et al.⁵⁰ [Colour figure can be viewed at wileyonlinelibrary.com]

investigation of the influence of the BPH,³⁸ of the heating temperature on residual stresses in SR heat treatments,⁴⁰ of size-effects,⁴⁴ of the stress ratio,⁴⁸ of the building orientation,^{42,44,48} and of the powder size.⁴⁹ In all the cases, the defects control the VHCF response and are responsible for the fatigue crack initiation. All the experimental results agree that the process parameters or the postprocesses allowing for a reduction of the defect size have a positive effect on the VHCF response. For example, BPH does not have a remarkable effect on the final porosity, and therefore, it mainly contributes to limit the scatter associated to the VHCF response and fosters the microstructure homogenization, but it does not permit a significant enhancement of VHCF response. Together with the defect size distribution, the microstructure can play a significant role. Indeed, the AB microstructure can be modified by varying the heating temperature in SR heat treatment. A heating temperature of 320°C in SR induces the rupture of the Si network and its spheroidization, with a consequent significant reduction of the Vickers hardness (about the half of the HV of AB specimens). The reduction of the HV induces a reduction of the VHCF strength, highlighting that also the microstructure is important when dealing with the VHCF response of material. On the other hand, by limiting the heating temperature in ST to 244°C, the Si network remains intact and the residual stresses are minimized, enhancing the VHCF response. Residual stresses are also important: SR heat treatment permitting to minimize residual stresses is beneficial, provided that the microstructure is not significantly altered. Moreover, all the researchers agree that the building orientation affects the VHCF response, which is largest for horizontally built specimens and decreases with the building angle. The reason is the different defect size and the larger defect range and scatter in vertically built specimens. According to Paolino et al.,⁴² defects in horizontally built specimens are mainly concentrated in the region where supports are removed; therefore, the removal of the external layer of the samples through a posttreatment (e.g., machining) eliminates the most defect-dense zones of the specimens, enhancing the final VHCF response. Size-effect is found to be relevant for both horizontally built and vertically built specimens: The experimental results in Tridello et al.⁴⁴ warns on the need of properly modeling size-effects when components are to be designed. As expected, moreover, the stress ratio affects the VHCF response, which decreases as the stress ratio increases. The powder size is another important parameter.⁴⁹ Indeed, the VHCF strength of specimens with larger powder size is larger than that of specimens manufactured with smaller powder size. The difference is related to the different size of the pores. As for the defect

population, in the case of nonmachined specimens, superficial and subsuperficial defects (pores, pore clusters, and LOF) are the most critical. In vertically built specimens, ILB defect type is critical too. On the other hand, for machined specimens, the VHCF failure can also initiate from internal defects, mainly pores with a critical diameter of around 40 μm . Typically, the machining process removes 1 mm of external layer. For AM components, in the external layer of material, the presence of defects is higher, and the defect size is larger compared with the internal defects. The presence of these large superficial defects drives the VHCF response, lowering the VCHF strength and leading to a premature failure. For this reason, machining is always suggested, when possible, to enhance the VHCF strength of the material. However, it must be noticed that for many real complex-shaped AM components, machining is not feasible and process-induced superficial defects must be considered during the fatigue design. Indeed, a difference in magnitude of about 50% can be present between VHCF strength of machined³⁸ and nonmachined⁴² specimens. In addition, the study shows that AlSi10Mg has better thermodynamic properties during the AM process providing a much more pore-free structure compared with AlSi12. The presence of Mg induces a grain refinement, the supersaturation of Si in Al matrix, and the Mg₂Si precipitation. In VHCF regime, finer grains and reduced porosity enhance related VHCF strength since they are the most effective combination to resist crack initiation. In Lesperance et al.,⁵⁰ a traditional T6 heat treatment is applied on machined specimens of AlSi10Mg. This post-process seems to improve the VHCF response of the material; however, further investigations about its effect on the microstructure and defect population are required. Finally, in Lesperance et al.⁵⁰ the VHCF response of AlSi7Mg alloy is investigated. The AlSi7Mg VHCF strength is smaller compared with its AlSi10Mg counterpart; however, the available experimental data are too small to draw reliable conclusions. Table 4 Summarizes the VHCF strength for each analyzed batch together with main process and testing parameters.

2.6 | VHCF strength of AlSi10Mg and AlSi7Mg: Summary

For the AlSi10Mg specimens, the influence of the BPH, of the heating temperature in SR heat treatments, of the building orientation, of residual stresses, and of the powder size is investigated:

- BPH (200°C) is suggested to avoid unexpected premature failures and mainly contributes to limit the

TABLE 4 VHCF strength of AM AlSi10Mg and AlSi7Mg depending on process setup

AlSi10Mg (SLM process)								
Specimen type	Building orient. ^a	Mechanical postprocess	Mean powder size (μm)	BPH (°C)	SR—oven cooling	Runout	Stress ratio <i>R</i>	VHCF strength (MPa)
H ³⁸	90°	mac	\	\	\	10 ⁸	−1	90
H ³⁸	90°	mac	\	200	\	10 ⁸	−1	90
G ³⁹	0°	pol	45	150	\	10 ⁹	−1	68
G ⁴⁰	0°	pol	45	150	320°C—2 h	10 ⁹	−1	61
G ⁴¹	0°	pol	45	150	244°C—2 h	10 ⁹	−1	76
G ⁴²	90°	pol	45	150	\	10 ⁹	−1	63
G ⁴⁴	0°	pol	45	150	\	10 ⁹	−1	68 ± 6.2
G ⁴⁴	90°	pol	45	150	\	10 ⁹	−1	55 ± 16
H ⁴⁴	0°	pol	45	150	\	10 ⁹	−1	97 ± 10
H ⁴⁴	90°	pol	45	150	\	10 ⁹	−1	68 ± 13
H ⁴⁸	0°	\	50	35	\	10 ⁹	−1	110
H ⁴⁸	0°	\	50	35	\	10 ⁹	0.5	51
H ⁴⁸	0°	\	50	35	\	10 ⁹	0	66
H ⁴⁸	90°	\	50	35	\	10 ⁹	−1	74
H ⁴⁸	90°	\	50	35	\	10 ⁹	0.5	34
H ⁴⁸	90°	\	50	35	\	10 ⁹	0	43
H ⁴⁹	0°	mac + pol	50	35	\	10 ⁹	−1	99
H ⁴⁹	0°	mac + pol	20	35	\	10 ⁹	−1	87
DG ⁵⁰	90°	mac	<63	180	T6	\	−1	94
AlSi7Mg (SLM process)								
DG ⁵⁰	90°	mac	<63	180	T6	\	−1	65

Abbreviations: BPH, base plate heating; H, hourglasses; DG, dog-bone; G, Gaussian; mac, final machining; pol, final polishing; SLM, selective laser melting; T6-traditional heat treatment T6 for aluminum alloy; VHCF, very high cycle fatigue.

^aAngle between building plate and specimen axis, that is, 90° vertical and 0° horizontal.

scatter associated to the VHCF results, but it does not permit a significant enhancement of VHCF response.

- SR (240°C—2 h) improves the VHCF strength, whereas SR (320°C—2 h) reduces it.
- Microstructure, together with defect size and residual stresses, influences the VHCF response: Heat treatments, which minimize the residual stresses but also involve a significant reduction of the Vickers hardness, could not be effective and could have a negative influence on the VHCF response.
- The building orientation influences the VHCF response: Horizontal specimens are characterized by a VHCF response better than that of vertically built specimens.
- The powder size influences the VHCF response: The VHCF strength of specimens produced with powder with mean size of 20 μm is smaller than that of specimens produced with powder with mean size of 50 μm.

- A traditional T6 heat treatment, together with BPH and machining, improves the VHCF response even if more analyses about the resulting microstructure and defect population are needed.

For the AlSi7Mg a limited number of experimental data are available, and it is difficult to draw reliable insights about the VHCF response of this alloy produced through AM. However, at a first glance, AlSi7Mg parts seem to have a VHCF strength smaller than that of AlSi10Mg parts.

3 | VHCF STRENGTH OF Ti6Al4V: EXPERIMENTAL RESULTS

In this section the results of experimental tests on the VHCF response of AM Ti6Al4V specimens are analyzed. In Wycisk⁵² the effect of different heat treatments and

postprocessing on Ti6Al4V alloy produced by means of SLM technology is investigated. A commercially available M270 manufacturing system (laser power 200W) and an alloy powder with a mean diameter of 41 μm by EOS company are employed for the production of the specimens. Two different batches are produced, named in this paper batch A and batch B, subjected to two different postprocesses. Batch A undergoes to an SR at 650°C for 3 h in vacuum, batch B is HIPed at 920°C and 1000 bar for 2 h. All the specimens are produced vertically and finally machined and manually polished. Fully reversed tension compression VHCF tests are carried out with an ultrasonic fatigue testing system, USF-2000 by Shimadzu, at a frequency of 20 kHz. The microstructure of batch A consists of fine α -phase and α' -martensite lamellae with size inferior to 1 μm and columnar grains of β -phase along the building direction. On the other hand, the HIP procedure removes the columnar structure, makes the α -lamellae (up to 4 μm) coarser, and induces the formation of a small amount of β -phase within the α -lamellae. More important, in batch B, prior observed gas porosities and process inherent defects are minimized or removed. Furthermore, a reduction in the yield strength and an increase in ductility is observed. The S-N plots of experimental data for batch A and batch B are shown in Figure 15A,B, respectively. As it can be noticed, the datasets show a monotonic decreasing trend, without a clear fatigue limit. In all the specimens, the crack initiates from internal defects. As for batch B, the reduction in defect population together with the homogenization of the microstructure leads to a highly improved VHCF strength and less scattered results. The graphically estimated VHCF strength up to 10^9 cycles of batch B is about 483 MPa, comparable with that of a traditional manufactured Ti alloy, whereas it is about 205 MPa for batch A, about 60% smaller. Overall, the HIP treatment is found to be extremely efficient in improving the VHCF response of the AM Ti6Al4V alloy.

In Gunther⁵³ the VHCF strength of additively produced Ti6Al4V alloys through SLM and EBM process is

investigated. Three different batches, named SLM-1b, SLM-2, and EBM, are produced. The first two batches are produced with an SLM process (SLM system by SLM Solution company). The alloy powder is composed of (wt %) 7.1 Al, 4.3 V and bal. with a mean diameter of around 42 μm . The building chamber (BPH) is heated up to 200°C, and a laser power of 400 W is employed. SLM-1b is heat-treated up to 800°C for 2 h, whereas SLM-2 is HIPed at 920°C and 1000 bar for 2 h in Ar atmosphere. As for the EBM batch, an Arcam A2X system by Arcam company is employed to manufacture the samples. The alloy powder is composed of (wt %) 7.3 Al, 4.5 V, and bal. with a mean diameter of around 73 μm . No postheat treatment is carried out on EBM samples. Raw cylinders are built vertically (SLM batches) and horizontally (EBM batch) and thereafter machined to the final tested hourglass geometry (gage diameter 4 mm). Lastly, all the samples are ground and polished before testing. The SEM investigation shows that the microstructure of SLM-1b and EBM is composed by a fine lamellar α -phase and minor amount of β -phase, whereas SLM-2 is composed by coarser partially spheroidized α -lamellae and interlamellar β -phase. Fully reversed tension compression VHCF tests are carried out with an ultrasonic fatigue testing system at a frequency of 19 kHz. Figure 16 shows the S-N plot of the experimentally tested batches together with literature results of tests carried out on Ti6Al4V specimens produced with traditional processes.⁵⁴ According to Figure 16, the graphically estimated VHCF strength up to 10^9 cycles of batch SLM-1b and EBM is very similar, around 275 MPa. Indeed, these two batches share almost the same microstructure and defect population. The critical defects are internal LOFs and pores. As for the SLM-2 batch, the graphically estimated VHCF strength up to 10^9 cycles is highly improved and nearly doubled compared with that of SLM-1b and EBM, around 435 MPa. The main reason is the homogenization of the structure and the minimization of the internal LOFs and pores through the HIP treatment, as already found in Wycisk et al.⁵² Accordingly, the crack

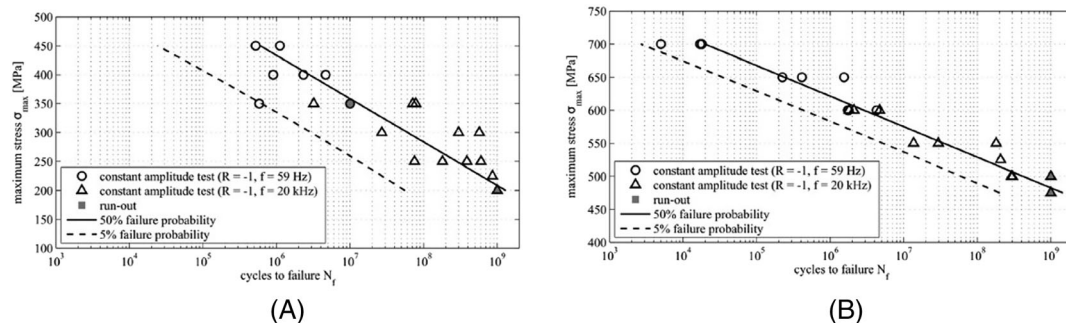


FIGURE 15 S-N plot of (A) batch A and (B) batch from Wycisk⁵²

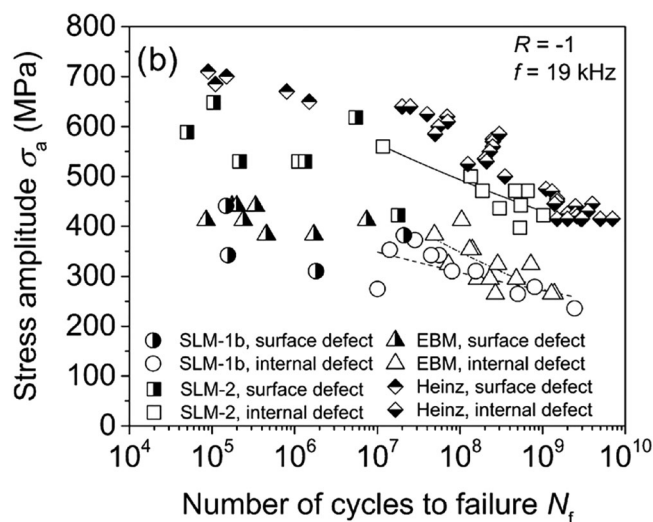


FIGURE 16 S-N plot of batch SLM 1b (SR), SLM-2 (HIP), EBM and conventional process by Heinz⁵⁴ batch from Gunther et al⁵³

mainly initiates at α -phase cluster and facets: In both cases, the applied stress for crack propagation is larger, thus justifying the enhanced VHCF response.

In Tridello et al.⁵⁵ the VHCF response of heat-treated SLM Ti6Al4V is experimentally assessed. A Renishaw AM400 system with laser power of 400 W, standard process parameters, and Ti6Al4V powder (mean diameter of 45 μm) are used to manufacture the tested AB Gaussian specimens⁵⁶ (risk volume of 2300 mm³). The specimens are vertically produced, then heat-treated at 850°C for 1 h followed by cooling in flowing Ar atmosphere and thereafter manually polished to reduce the surface roughness and avoid premature HCF failures due to large surface defects. Two self-assembled ultrasonic fatigue testing machines (UFTMs) are employed for the VHCF tests up to 10⁹ cycles. The microstructure is mainly composed of α -lamellae and local β -phase. The S-N plot of experimental data with respect to s_{local} is shown in Figure 17. The results show a large scatter, and a clear monotonic decreasing trend is not visible and the VHCF strength is concentrated in the range 145–200 MPa. Critical defects are ILBs and LOFs, 80% superficial and subsuperficial and 20% located internally. Depending on the defect location, the VHCF response changes remarkably: According to Figure 17, the two failures originated from internal defects are characterized by a fatigue life significantly larger (2 orders of magnitude) than the fatigue life of the failure originated at a surface defect and subjected to the same applies stress amplitude. Therefore, the removal of an external layer of material can enhance VHCF response.

Du et al.⁵⁷ investigate the influence of the SLM process parameters on the VHCF response of Ti6Al4V. A

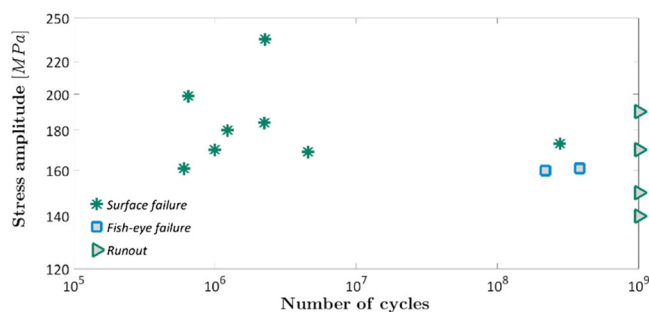


FIGURE 17 Stress-life (S-N) plot of the experimental data obtained considering s_{local} from Tridello et al⁵⁵ [Colour figure can be viewed at wileyonlinelibrary.com]

commercially available HBD-200 SLM machine with a maximum power of 200 W is employed for the specimen production. The scanning procedure firstly defines the section contour in the layer and then proceeds with infilling the inner areas. The laser travel direction for the infill scanning is rotated by 60° in each subsequent layer. An SR at 600°C for 2 h followed by flowing Ar cooling is applied to all specimens, which are finally polished to reduce roughness. The alloy powder is composed of (wt %) 6.40 Al, 4.1 V, 0.01 C, 0.19 Fe, 0.01 N, and bal. with a mean diameter of around 34 μm . Vertical hour-glasses specimens (gage diameter 3.5 mm) are subjected to fully reversed tension compression VHCF tests up to 10⁹ cycles with a Lasur GF20-TC ultrasonic testing system (loading frequency of 20 kHz). The achieved microstructure of SLM Ti6Al4V is deeply detailed in previous studies.^{58,59} An orthogonal design of experiments (OED) with nine different batches is carried out to assess the effect of the main four process parameters, namely, laser power P (W), hatching distance h (mm), layer thickness t (μm), and scan speed v (mm/s). Figure 18A shows the relationship between the final porosity and the selected process parameters, whose influence follows the order: laser power > hatching distance > layer thickness > and scan speed. The optimal parameters combination, used for the production of an additional validation batch numbered 10, results to be: laser power of 160 W, hatching distance of 0.07 mm, layer thickness of 30 μm , and scan speed of 1000 mm/s. As for the VHCF response, Figure 18B shows the S-N plot of some of the most significant batches. For the highest values of porosity (8.03%, worst-case scenario) the graphically estimated VHCF strength up to 10⁹ cycles is the lowest (about 95 MPa), whereas in the validation group, characterized by the lowest porosity density, (0.20%, best case scenario), the graphically estimated VHCF strength up to 10⁹ cycles is the highest, about 215 MPa. The most critical defects in the VHCF regime are subsuperficial LOFs, which form mainly due to a bad combination of process parameters,

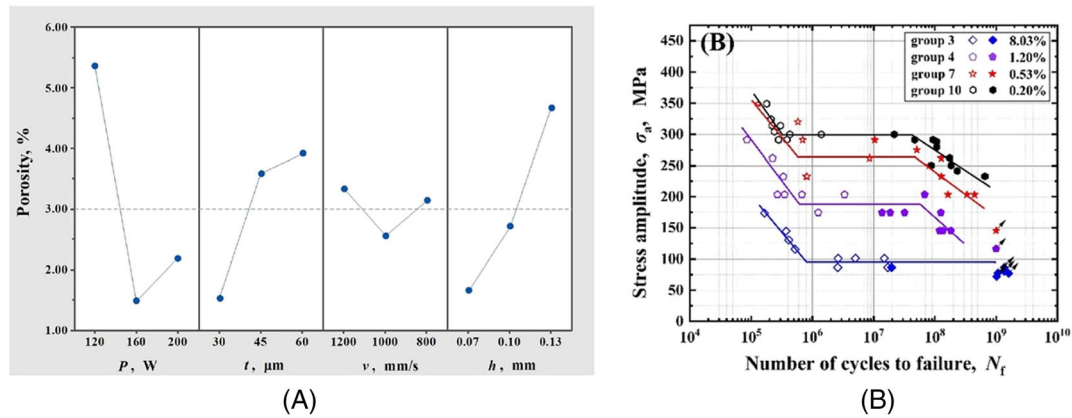


FIGURE 18 Very high cycle fatigue (VHCF) response from Du et al.⁵⁷: (A) porosity versus process parameters; (B) stress-life (S-N) plot. Note: (B) full dense marks indicate crack initiation from subsurface or internal defects, hollow marks from surface defects and with arrows are run outs. Group 10 is the reference batch and the value in percentage indicates the related porosity [Colour figure can be viewed at wileyonlinelibrary.com]

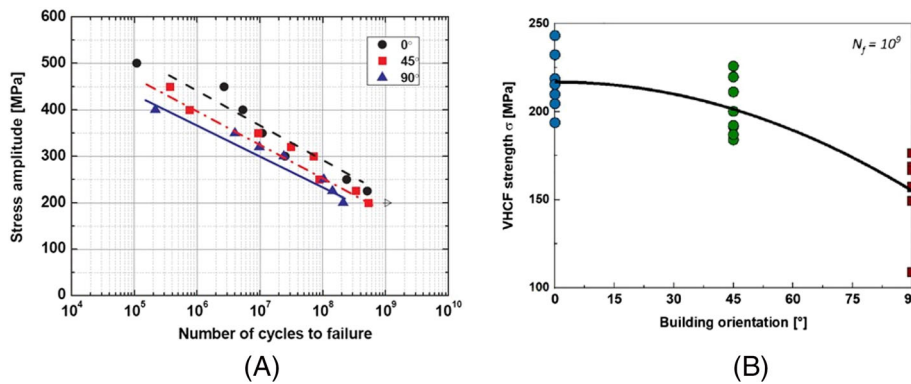


FIGURE 19 Very high cycle fatigue (VHCF) response from Qian et al.⁶⁰: (A) stress-life (S-N) plot and (B) effect of building orientation on fatigue strength at 10^9 cycles [Colour figure can be viewed at wileyonlinelibrary.com]

such as insufficient laser power for a selected hatching distance or layer thickness.

Qian, in,⁶⁰ studies the VHCF response of SLM Ti6Al4V samples built with different orientations. A Lasur GF20-TC ultrasonic testing system (loading frequency of 20 kHz) is used for fully reversed tension compression VHCF tests. Raw cylinders are manufactured in three directions with respect to the building plate, namely, 0°, 45°, and 90°. Afterwards, all the specimens are machined to the final hourglass geometry (gage diameter 3.5 mm) for VHCF tests. The typical lamellar microstructure of Ti-6Al-4 V processed by SLM is obtained. Figure 19A shows the S-N plot of different batches. As it can be noticed, specimens built with 0° building orientation are characterized by the best VHCF response, whereas the VHCF response of specimens built at 90° is the worst. The slope of the three curves is similar, and no evident stepwise type of S-N data is present. The crack initiates at internal LOF defects or pores caused by the SLM process both in HCF and VHCF regime. The effect of different building orientations is more evident in the

HCF regime. The difference in fatigue strength is due to the presence of larger defects in the 90° batch. The median value of the VHCF strength at 10^9 cycles is 217 MPa for the 0° batch, followed by 210 MPa for the 45° batch and finally 155 MPa for the 90° batch, with a reduction of 40% from 0° to 90°. In Figure 19B the authors analyze the VHCF strength decrement at 10^9 cycles with respect to the building orientation angle. A quadratic model is used to fit the experimental data.

In Liu et al.,⁶¹ the VHCF response and the defect population of AB SLM Ti6Al4V specimens are investigated. The specimens are produced with a laser power of 500 W and BPH at 60°C. The alloy powder is composed of (wt %) 5.99 Al, 3.49 V, and bal. and has a mean diameter of around 33 μm. Fully reversed tension compression VHCF tests at 20 kHz are carried out with an USF-2000 (Shimadzu) ultrasonic testing system. Raw cylinders are at first produced in vertical direction and afterwards machined and polished to the hourglass geometry (gage diameter 3 mm). The microstructure is mainly composed of acicular α and α' lamellae and columnar β -phase along

building axis. Figure 20 shows the fatigue response (S-N plot) of the specimens. As it can be noticed, an evident VHCF limit is not observable, whereas a steady decrease in strength with increasing lifetime to failure is present. The VHCF strength is assessed to be around 285 MPa at 10^9 cycles. For more, VHCF failures mainly originate from subsuperficial or internal LOF defects due to local process instabilities. Compared with the traditionally manufactured alloy in Heinz and Eifler,⁶² the VHCF is almost halved due to these internal SLM-induced defects. In the VHCF regime, the defect shape is usually regular and spherical.

In Liu et al.⁶³ the EBM-induced anisotropy and the related VHCF response of Ti6Al4V are investigated. A Q10 system by Arcam company is employed to manufacture the samples. The building chamber is heated at 587°C, and it is kept under vacuum at $7.8 \cdot 10^{-3}$ mbar. Two different batches are built, named in the paper *xoy* and *xoz*. Raw cuboids *xoy* and *xoz*, produced through EBM in horizontal and in vertical directions, respectively, are machined and polished to the tested hourglass geometry (gage diameter 3 mm). The surfaces parallel to the vertical direction present a very high roughness, about R_a equal to 35 μm , due to the large presence of nonmelt particles partly sintered to the surface. Due to the high temperature in the chamber, the AB structure with fine acicular α -phase and α' -martensite with small amount of β -phase is transformed in a coarser duplex phase $\alpha + \beta$. Elongated columnar grains of β -phase are observable along the building direction, improving the ductility in

this direction. However, these microstructural changes are not effective for top layers that present a microstructure closer to that AB. Indeed, these layers spend a smaller time in the heated chamber before the process end. Figure 21 shows the S-N plot of the *xoy* batch, that is, horizontally built. A transition stress between HCF and VHCF failures at about 450 MPa is observable in the S-N plot, and the graphically estimated VHCF strength up to 10^9 cycles is close to 260 MPa. At number of cycles smaller than 10^7 , the critical defects are superficial, whereas internal pores are the responsible for the crack initiation in the VHCF region. In this case, the porosity is not caused by shield gas inclusion, because the EBM process is carried out under high vacuum. The pores are instead produced by the Al vaporization present in the alloy powder during the process.

3.1 | VHCF strength of Ti6Al4V: Discussion

Table 5 lists the literature results on the VHCF response of AM Ti6Al4V alloys.

In two works, the influence of the HIP treatment is investigated, proving that it has a positive influence on the VHCF response. Indeed, the HIP procedure homogenizes the structure and closes or removes most of the process-induced defects. The graphically estimated VHCF strength up to 10^9 cycles of specimens subjected to HIP process is within the range 400–500 MPa, and it is close to that of traditionally manufactured Ti alloy. AB EBM samples and SLM + SR treated samples share almost the same microstructure and defect population. As a matter of fact, the SR

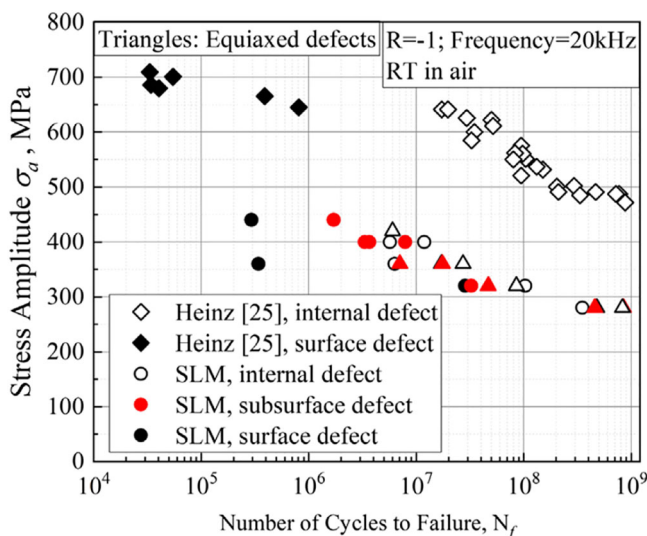


FIGURE 20 Stress-life (S-N) plot of experimental data from Liu et al.⁶¹ Note: Beretta and Romano²⁵ in the legend refers to traditionally manufactured Ti6Al4V alloy. In the present paper the reference is Heinz and Eifler⁶² [Colour figure can be viewed at wileyonlinelibrary.com]

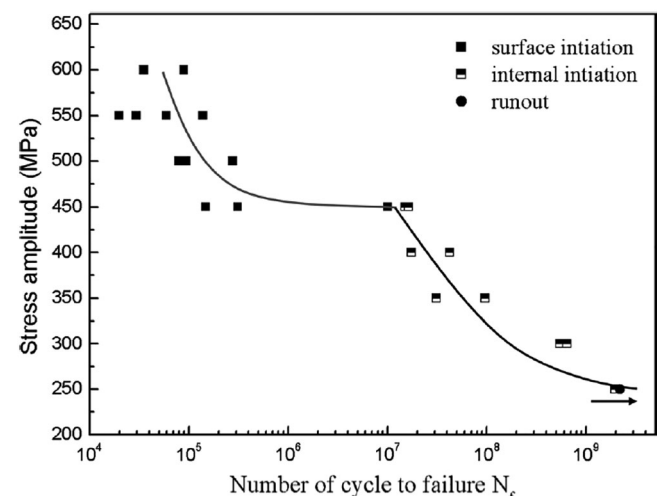


FIGURE 21 Stress-life (S-N) plot of experimental data from Liu et al.⁶³

TABLE 5 VHCF strength of AM Ti6Al4V depending on process setup

Ti6Al4V					
Specimen type	Process	Building orient. ^a	Mechanical postprocess	Thermal postprocess	VHCF strength (MPa)
H ⁵²	SLM	90°	mac + pol	SR 650°C—3 h	205
H ⁵²	SLM	90°	mac + pol	HIP 920°C 100 MPa—2 h	483
H ⁵³	SLM (BPH 200°C)	90°	mac + pol	SR 800°C—3 h	240
H ⁵³	SLM (BPH 200°C)	90°	mac + pol	HIP 920°C 100 MPa—2 h	435
H ⁵³	EBM	0°	mac + pol	\	275
G ⁵⁵	SLM	90°	pol	SR 850°C—1 h	150
H ⁵⁷	SLM (OCS)	90°	pol	SR 600°C—2 h	215
H ⁵⁷	SLM (WCS)	90°	pol	SR 600°C—2 h	95
H ⁶⁰	SLM	0°	mac	\	217
H ⁶⁰	SLM	45°	mac		210
H ⁶⁰	SLM	90°	mac		155
H ⁶¹	SLM (BPH 60°C)	90°	mac + pol	\	285
H ⁶³	EBM (BPH 587°C)	0°	mac + pol	\	260

Abbreviations: BPH, base plate heating; EBM, electron beam melting; G, Gaussian; H, hourglasses; mac, final machining; OCS, optimal case scenario, that is, optimized choice of process parameters; pol, final manual polishing; SLM, selective laser melting; VHCF, very high cycle fatigue; WCS, worst-case scenario.

^aAngle between building plate and specimen axis, that is, 90° vertical and 0° horizontal.

effect is partly included in the EBM process where the building chamber is heated up to 500–600°C. Nevertheless, the EBM process induces higher anisotropy along the building direction due to different time of exposure to high temperature of melt layers. Anyway, the VHCF strength of SLM + SR and EBM is within the range of 150–285 MPa, almost half of HIPed specimens. The most critical defects are mainly internal LOFs and pores caused by process instabilities. Indeed, a bad combination of process parameters can increase the defect population and lower of about 40% of the VHCF strength. Similarly, the building direction can reduce the VHCF strength by about 40% from horizontally to vertically built specimens. The SR treatment and machining postprocess increase the VHCF strength, but it seems not to be that effective as for the AlSi10Mg alloy. The use of Gaussian specimens leads to a more conservative estimation of VHCF strength due to larger employed risk volume. Overall, the most effective way to enhance the VHCF strength of Ti6Al4V is by means of HIP postprocess,⁵³ together with a proper selection of process parameters, as investigated in Du et al.⁵⁷ The optimal SLM process parameters combination results to be laser power of 160 W, hatching distance of 0.07 mm, layer thickness of 30 μm, and scan speed of 1000 mm/s.

3.2 | VHCF strength of Ti6Al4V: Summary

For the Ti6Al4V specimens, the influence of the production processes (SLM and EBM), of heat treatments, and of the HIP process is mainly investigated:

- HIP enhances the VHCF strength, becoming comparable with that of traditionally manufactured Ti alloy.
- AB EBM samples and SLM + SR treated samples share almost the same VHCF strength.
- EBM process induces higher anisotropy along the building direction.
- The VHCF strength of vertically built specimens is in average 40% lower than that of horizontally built specimens.

4 | VHCF RESPONSE OF INCONEL 718: EXPERIMENTAL RESULTS

In Yang et al.,⁶⁴ the VHCF response of SLM Inconel 718 in the AB condition is investigated. An SLM system M290 by EOS GmbH company with laser power of 285 W is employed, for manufacturing, in vertical direction, raw cylinders, which are thereafter machined and polished to the final tested hourglass geometry (gage diameter

3 mm). Fully reversed tension compression VHCF tests are carried out with an ultrasonic fatigue testing system, USF-2000 by Shimadzu, at a loading frequency of 20 kHz. The microstructure is characterized by a fine dendritic structure with dendritic arm spacing (DAS) of about $0.8\ \mu\text{m}$, elongated in the building direction. The interdendritic regions are mainly constituted by a large amount of granular precipitates composed of Laves phases. Figure 22 shows the S-N plot of the experimental data. As it can be noticed, a clear fatigue limit does not exist as in traditional manufactured Inconel 718.⁶⁵ Two main slopes are clearly visible, discriminating between two failure modes: failures from surface defects in the HCF region (black curve on the left) and failures from internal defects in the VHCF region (red curve on the right). The graphically estimated VHCF strength at 10^9 cycle is approximately 432 MPa. Three main types of defects are observed through SEM analysis, namely, pores, LOFs, and crystallographic facets. However, LOF defects are rare and mainly formed due to bad process parameters combination, according to the authors. On the other hand, pores are quite frequent and together with crystallographic facets simultaneously cause the crack initiation in most of the cases.

The VHCF response of wrought and SLM heat-treated Inconel 718 is investigated in Voloskov et al.⁶⁶ The study focuses on the influence of test frequency and building orientation. An SLM system M290 by EOS company with laser power of 285 W is employed. Hourglass specimens are manufactured vertically and at 45° with respect to the base plate, with material allowance for the subsequent machining process. Afterwards, the AB specimens are heat-treated for 10 min at 954°C , then for 8 h at 718°C , and finally for 10 h at 621°C . Before testing, the specimens are finally machined and polished (gage diameter

of 3 mm). A second batch of wrought specimens is tested: In this case, the same hourglass geometry is obtained by machining round bars processed and heat-treated according to SAE ANS2774E. Fully reversed tension compression VHCF tests are carried out with an ultrasonic fatigue testing system, USF-2000 by Shimadzu, at a loading frequency of 20 kHz. Figure 23 shows the experimental data of the three tested batches, namely, vertically built (V-SLM), diagonally built (D-SLM), and wrought (W). The SLM specimens are characterized by a fatigue response at high stress levels (in the HCF region) better than that of W specimens. At lower stress levels (in the VHCF region), the difference tends to diminish and the VHCF strength of V-SLM specimens is larger than that of D-SLM specimens. The difference between the fatigue strength of W and SLM specimens is due to the large static strength and hardness of SLM specimens. The different fatigue response of the two tested SLM batches (i.e., manufactured with different building directions) can be explained by considering the microstructures and crack initiation sites. In both the SLM microstructures, a dendritic structure elongated in the building direction within coarse columnar grains, similarly to the AB condition found in Yang et al.,⁶⁴ is present. The crack originates from persistent slip bands (PSBs) within the elongated grains oriented at around 45° with respect to the loading axis. The probability of slip planes in that direction for D-SLM specimens is larger, being detrimental for the fatigue life. Interestingly, even if pores are present (35 pores per mm^3 , mostly with diameter $<15\ \mu\text{m}$), the critical defects are PSBs. The small defect density could be also due to the small risk volume of the tested hourglass specimens. The graphically estimated mean VHCF strength at 10^9 cycles for V-SLM and D-SLM is approximately 334 and 245 MPa, respectively.

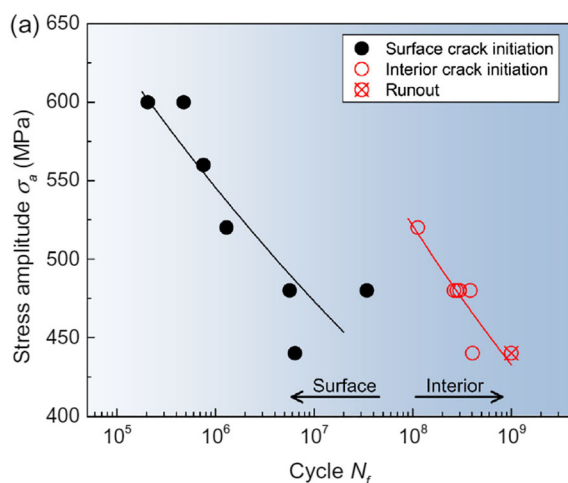


FIGURE 22 Stress-life (S-N) plot of experimental data from Yang et al.⁶⁴ [Colour figure can be viewed at wileyonlinelibrary.com]

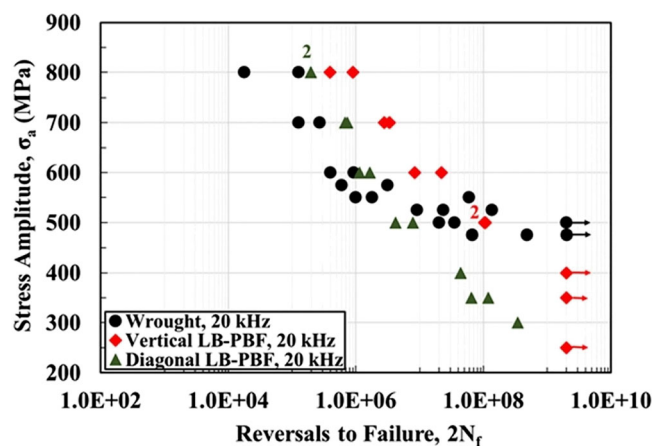


FIGURE 23 Stress-life (S-N) plot of experimental data from Muhammad et al.⁶⁶ [Colour figure can be viewed at wileyonlinelibrary.com]

The influence of the loading frequency on the tested Inconel 718 is also verified in the paper, showing that ultrasonic testing can overestimate the fatigue strength of the material. Indeed, in ultrasonic tests, the specimen is considered to behave following the linear elastic model. However, during the test, plasticity phenomena can appear, and the estimated resonance frequency may not be accurate anymore, according to the explanation of the authors. The authors therefore proposed the following correction factor for test results obtained with the ultrasonic testing machines:

$$\sigma_{UF}^C = 0.85 \times \sigma_{UF}, \quad (2)$$

where σ_{UF}^C is the corrected stress amplitude and σ_{UF} is the measured one.

The subsurface cracking mode with fisheye pattern of SLM Ni-based superalloy (Inconel 718) in the VHCF regime is investigated by Li et al.⁶⁷ An SLM system M280 by EOS company with laser power of 280 W is employed. The Ni-based superalloy powder is composed of (wt %) 52.16 Ni, 19.34 Cr, 5.07 Nb, 2.96 Mo, 0.89 Ti, 0.51 Al, 0.049 Co, 0.0041 C, and 0.0021 Mn with a maximum particle size below 40 μm . Raw cylinders are manufactured vertically without further heat treatment. Afterwards, the cylinders are machined and grounded to the final hour-glass testing shape (gage diameter 4 mm). The VHCF strength is evaluated with axial loading fatigue tests at stress ratio R equal to 0.1 by using an electromagnetic resonant testing machine at a frequency of 100 Hz. The AB microstructure is similar to that found in Yang et al.,⁶⁴ characterized by a very fine cellular structure in the plane parallel to the building plate. Figure 24A shows the S-N plot up to 10^8 cycles together with a linear fitting

curve. The graphically estimated VHCF strength at 10^9 cycles is around 500 MPa. However, the experimental data do not show a clear transition between the HCF and VHCF regime, with a monotonic decreasing trend from the HCF to the VHCF region. VHCF failures mainly originate from internal nonmetallic inclusions or pores, with a subsequent progressive crack propagation. Figure 24B shows precisely how this mechanism takes place in the SLM Ni-based superalloy.

Initially, the crack initiates from grain slip assisted by inclusion along the maximum shear stress plane. Then, the microcrack grows and induces the formation of facets. Finally, this process continues forming the well-known circular fisheye pattern till the specimen collapses.

4.1 | VHCF response of Inconel 718: Discussion

AM-produced Inconel 718 exhibits a very good fatigue response. In the VHCF response, some peculiar aspects can be inferred from the literature data. First of all, differently from tests on traditionally built Inconel 718 specimens, a clear fatigue limit is not present. Secondly, the critical defects are always internal and mainly nonmetallic inclusions, pores, and LOFs together with facets and crystallographic discontinuities. Finally, the heat treatment seems not to improve remarkably the VHCF response. In contrast with other AM materials, such as Ti6Al4V⁶⁰ and AlSi10Mg,⁴² the vertically built Inconel 718 specimens do not present a decrease in fatigue performance. On the contrary, the vertical build direction guarantees a good VHCF strength at 10^9 cycles, while it

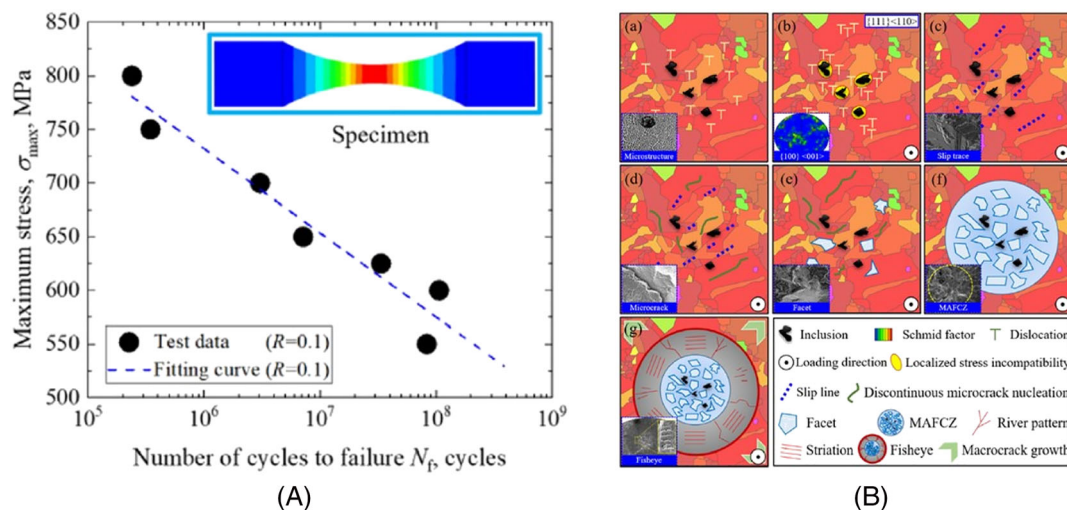


FIGURE 24 (A) Stress-life (S-N) plot of experimental data and (B) fisheye formation process from internal defects⁶⁷ [Colour figure can be viewed at wileyonlinelibrary.com]

TABLE 6 VHCF strength of AM IN718 depending on process setup

Inconel 718 (SLM process, final machining and polishing)					
Specimen type	Building orientation ^a	Thermal postprocess	Stress ratio <i>R</i>	Runout	VHCF strength (MPa)
Hourglass ⁶⁴	90°		-1	10 ⁹	432
Hourglass ⁶⁶	90°	1) 954°C—10 min 2) 718°C—8 h 3) 621°C—10 h	-1	10 ⁹	334
Hourglass ⁶⁶	45°	1) 954°C—10 min 2) 718°C—8 h 3) 621°C—10 h	-1	10 ⁹	246
Hourglass ⁶⁷	90°	\	0.1	10 ⁸	500

Abbreviations: SLM, selective laser melting; VHCF, very high cycle fatigue.

^aAngle between building plate and specimen axis, that is, 90° vertical and 0° horizontal.

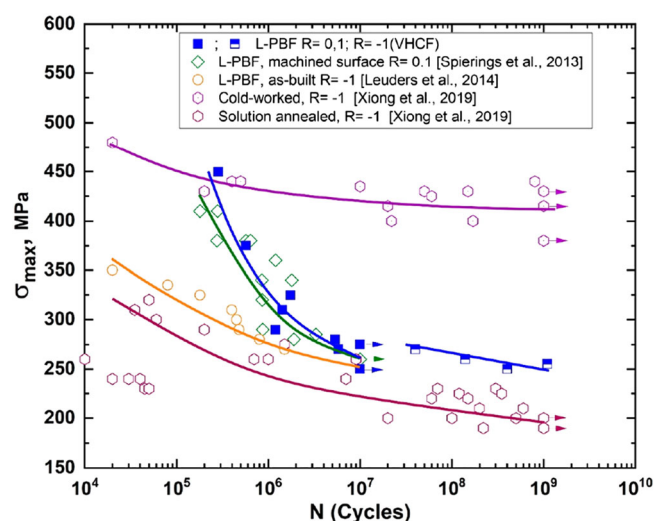


FIGURE 25 Stress-life (S-N) plot of experimental data from Voloskov et al.⁶⁸ Note: The references to Spierings 2013, Leuders 2014, and Xiong 2019 in the plot are in this paper numbered,^{69–71} respectively [Colour figure can be viewed at [wileyonlinelibrary.com](https://onlinelibrary.wiley.com)]

is highly reduced in diagonally built specimens. Moreover, in Muhammad et al.⁶⁶ two aspects are highlighted by the authors: Firstly, the need of enlarging the tested risk volume, since the hourglass shape does not permit to properly assess the defects population, and consequently, to reliably estimate the VHCF response (as already noticed for AlSi10Mg in Tridello et al.⁴⁴). Secondly, when ultrasonic fatigue tests are carried out, possible strain rate effects and plastic phenomena should be verified and considered, in order to avoid an overestimation of the VHCF response.

Table 6 summarizes the experimental results of VHCF tests on the Inconel 718 alloy: The main process parameters and the VHCF strength are reported.

4.2 | VHCF response of Inconel 718: Summary

For the specimens produced with the Inconel 718 alloy, the influence of defects and building orientation is mainly investigated:

- Differently from traditionally built specimens, no clear VHCF limit is present, whereas a monotonically decreasing behavior takes place.
- The critical defects are mainly facets and crystallographic discontinuities.
- VHCF strength is highly reduced in specimens built at 45° built compared with vertically built ones.

5 | VHCF RESPONSE OF 316L STAINLESS STEEL: EXPERIMENTAL RESULTS AND DISCUSSION

The VHCF response of SLM stainless steel 316L is studied in Voloskov et al.⁶⁸ An SLM system TruPrint1000 by Trumpf company with laser power of 113 W is used. The diameter of the 316L gas atomized powders is in the range 20–50 μm. Raw cylinders are manufactured vertically and thereafter machined and ground to the final hourglass testing shape (gage diameter 3 mm). Fully reversed tension compression VHCF tests are carried out with an ultrasonic fatigue testing system, USF-2000 by Shimadzu, at a loading frequency of 20 kHz. Figure 25 shows the S-N plot of the experimental data together with literature results on cold-worked and heat-treated stainless steel. The VHCF response of SLM 316L is better than that of the annealed batch but the half of that of cold-worked specimens.

The VHCF strength at 10^9 cycles is around 250 MPa, and the trend is monotonically decreasing without an evident fatigue limit in the VHCF region. The critical defects are internal nonmetallic inclusions and LOF defects, which originate a fisheye morphology on the fracture surface.

5.1 | VHCF response of 316L stainless steel: Summary

One work is published on the VHCF response of SLM 316L specimens, comparing the VHCF response of AM specimens with that of traditionally built specimens:

- The VHCF response of SLM 316L is better than that of traditional annealed stainless steel, but the half of that of cold-worked specimens.
- The VHCF response presents a monotonically decreasing trend without an evident fatigue limit.

6 | CONCLUSIONS

In the present paper, a literature review on the VHCF response of specimens produced through AM processes is provided. To guarantee a safe design of the components produced through AM, the fatigue response at very high number of cycles should be also reliably assessed. The growing importance of the research on the VHCF response of parts produced through AM processes is attested by the increment of papers published on this subject in the last 2 years (2019–2020), being about the 60% of the total. However, more efforts should be made to understand the mechanisms of crack initiation and the influence of process parameters and post-treatments on the VHCF response of AM parts.

At present, SLM and EBM production processes are used to manufacture specimens for VHCF tests. EBM samples are tested in the VHCF regime only for Ti6Al4V. The results show that the EBM process produces the final part which behaves similarly to heat-treated SLM ones with increased building direction anisotropy. Applied laser power, printing speed, hatching distance, and the other process parameters are studied deeper only for Ti6Al4V. However, these parameters and their correct combination are almost always suggested by the machine producers. For most of the tested alloys, the default process setup is employed. Indeed, this setup is often guaranteeing the lower defect density and relative porosity. As for the powder size, for all the studied alloys, the mean diameter of the atomized powder should be around 50 μm . Inferior values induced more gas inclusions and larger defects.

For what concerns the experimental tests, they are mainly carried out with Ti6Al4V and AlSi10Mg specimens, whereas a smaller number of results are available for AlSi12, IN718, and 316L specimens. Experimental tests are mainly carried out by using ultrasonic testing machines working at a loading frequency in the range 19–21 kHz, but experimental tests with traditionally testing machines are also carried out to assess the influence of the loading frequency. The process-induced defects, such as LOFs, pores, and ILBs, control the VHCF response for every studied alloy. If defects are not present or are removed with post-treatments, the microstructural defects are responsible for the fatigue crack initiation. It has been found that the most defect-dense zone is close to the AB surface. Therefore, the removal through machining of this zone would eliminate the largest defects and would surely have a positive effect on the VHCF response. Anyway, this operation may induce an incorrect evaluation of the fatigue limit of real parts. For example, if a part of an AM component would not be reached by matching tools, a consistent part of the surface would remain untouched. This phenomenon may be frequent since AM components are often characterized by convoluted and complex geometries. The unmachined surface would induce a premature fatigue failure compared with the data from machined samples. Hence, the final machining and polishing must be considered as crucial operations in the evaluation of the VHCF strength. Similarly, the properly estimation of the defect population and consequently of the VHCF response requires an enlargement of the tested risk volume to avoid underestimation of the critical defect size. Otherwise, a larger number of experimental tests should be carried out.

All considered, differently from VHCF results on specimens produced through traditional processes, the fatigue failures in VHCF parts do not originate from internal defects with a fisheye morphology for all the tested AM materials, depending on the location of the initial defect and on the density of defects within the specimen section. To conclude, according to the analyses carried out in the paper and based on literature results, the effects of heat process parameters and post-treatments are extensively investigated for Ti6Al4V and AlSi10Mg specimens. However, there is the need to fill the gap of knowledge regarding the effect of process parameters and post-treatments for other commercially available materials to be produced with the AM processes. Indeed, due to the large number of process parameters involved in the specimen production, the extension of the main findings for a specific material could not be valid for other materials, making it necessary an accurate experimental validation. The research should also focus on the mechanisms of crack initiation in parts produced

through AM, to provide reliable design procedures and to verify if the traditional design methodologies can be applied even for AM components.

ACKNOWLEDGMENTS

Open Access Funding provided by Politecnico di Torino within the CRUI-CARE Agreement.

CONFLICT OF INTEREST

The authors declared that there is no conflict of interest.

AUTHOR CONTRIBUTIONS

R. Caivano: retrieved the literature data, analyzed the data, and wrote the paper. **A. Tridello:** helps analyzing the data, made additions to the paper, and revised the paper. **G. Chiandussi and G. Qian:** revised the paper. **D. S Paolino:** revised the manuscript and supervised the work. **F. Berto:** revised the manuscript and supervised the work.


DATA AVAILABILITY STATEMENT

The authors confirm that the data supporting the findings of this study are available within the article and its supporting information.

ORCID

Riccardo Caivano  <https://orcid.org/0000-0002-5030-1579>

Andrea Tridello  <https://orcid.org/0000-0003-3007-3377>

Giorgio Chiandussi  <https://orcid.org/0000-0001-9273-1094>

Guian Qian  <https://orcid.org/0000-0003-0487-9780>

Davide Paolino  <https://orcid.org/0000-0002-4231-4580>

Filippo Berto  <https://orcid.org/0000-0001-9676-9970>

REFERENCES

- Oztan C, Coverstone V. Utilization of additive manufacturing in hybrid rocket technology: A review. *Acta Astronaut.* 2021; 180:130-140.
- Liu G, Zhang X, Chen X, et al. Additive manufacturing of structural materials. *Mater Sci Eng R Reports.* 2021;145:100596.
- Yusuf SM, Cutler S, Gao N. Review : The impact of metal additive. *Metals (Basel).* 2019;1:35.
- Gisario A, Kazarian M, Martina F, Mehrpouya M. Metal additive manufacturing in the commercial aviation industry: A review. *J Manuf Syst.* 2019;53:124-149.
- Al Rashid A, Khan SA, G. Al-Ghamdi S, Koç M. Additive manufacturing: Technology, applications, markets, and opportunities for the built environment. *Autom Constr.* 2020;118: 103268.
- Juechter V, Franke MM, Merenda T, Stich A, Körner C, Singer RF. Additive manufacturing of Ti-45Al-4Nb-C by selective electron beam melting for automotive applications. *Addit Manuf.* 2018;22:118-126.
- Rezvani Ghomi E, Khosravi F, Neisiany RE, Singh S, Ramakrishna S. Future of additive manufacturing in healthcare. *Curr Opin Biomed Eng.* 2021;17:100255.
- Buj-Corral I, Tejo-Otero A, Fenollosa-Artés F. Development of am technologies for metals in the sector of medical implants. *Metals (Basel).* 2020;10:1-30.
- Tiwari R, Andhare RS, Shooshtari A, Ohadi M. Development of an additive manufacturing-enabled compact manifold microchannel heat exchanger. *Appl Therm Eng.* 2019;147: 781-788.
- Caivano R, Tridello A, Codegone M, Chiandussi G. A new methodology for thermostructural topology optimization: Analytical definition and validation. *Proc Inst Mech Eng Part L J Mater des Appl.* 2020;1-20.
- Singh S, Ramakrishna S. Biomedical applications of additive manufacturing: Present and future. *Curr Opin Biomed Eng.* 2017;2:105-115.
- Allevi G, Cibeca M, Fioretti R, Marsili R, Montanini R, Rossi G. Qualification of additively manufactured aerospace brackets: A comparison between thermoelastic stress analysis and theoretical results. *Meas J Int Meas Confed.* 2018;126:252-258.
- Brusa E, Sesana R, Ossola E. Numerical modeling and testing of mechanical behavior of AM Titanium alloy bracket for aerospace applications. *Procedia Struct Integr.* 2017;5:753-760.
- Cooke S, Ahmadi K, Willerth S, Herring R. Metal additive manufacturing: Technology, metallurgy and modelling. *J Manuf Process.* 2020;57:978-1003.
- Yadollahi A, Shamsaei N. Additive manufacturing of fatigue resistant materials: Challenges and opportunities. *Int J Fatigue.* 2017;98:14-31.
- Romano S, Brückner-Foit A, Brandão A, Gumpinger J, Ghidini T, Beretta S. Fatigue properties of AlSi10Mg obtained by additive manufacturing: Defect-based modelling and prediction of fatigue strength. *Eng Fract Mech.* 2018;187:165-189.
- Frazier WE. Metal additive manufacturing: A review. *J Mater Eng Perform.* 2014;23(6):1917-1928.
- Agius D, Kourousis KI, Wallbrink C. A review of the as-built SLM Ti-6Al-4V mechanical properties towards achieving fatigue resistant designs. *Metals (Basel).* 2018;8:1-25.
- Hack H, Link R, Knudsen E, Baker B, Olig S. Mechanical properties of additive manufactured nickel alloy 625. *Addit Manuf.* 2017;14:105-115.
- Kempen K, Thijs L, Van Humbeeck J, Kruth JP. Mechanical properties of AlSi10Mg produced by selective laser melting. *Phys Procedia.* 2012;39:439-446.
- Suryawanshi J, Prashanth KG, Ramamurty U. Mechanical behavior of selective laser melted 316L stainless steel. *Mater Sci Eng A.* 2017;696:113-121.
- Shrestha S, Panakarajupally RP, Kannan M, Morscher G, Gyekenyesi AL, Scott-Emuakpor OE. Analysis of microstructure and mechanical properties of additive repaired Ti-6Al-4V by Direct Energy Deposition. *Mater Sci Eng A.* 2021;806: 140604.
- Yamashita Y, Murakami T, Mihara R, Okada M, Murakami Y. Defect analysis and fatigue design basis for Ni-based superalloy 718 manufactured by selective laser melting. *Int J Fatigue.* 2018;117:485-495.
- Jalalahmadi B, Liu J, Liu Z, Vechart A, Weinzapfel N. An integrated computational materials engineering predictive

- platform for fatigue prediction and qualification of metallic parts built with additive manufacturing. *J Tribol.* 2021;143(5):1-22.
25. Beretta S, Romano S. A comparison of fatigue strength sensitivity to defects for materials manufactured by AM or traditional processes. *Int J Fatigue.* 2017;94:178-191.
 26. Marines I, Bin X, Bathias C. An understanding of very high cycle fatigue of metals. *Int J Fatigue.* 2003;25(9-11):1101-1107.
 27. Bathias C. There is no infinite fatigue life in metallic materials. *Fatigue Fract Eng Mater Struct.* 1999;22(7):559-565.
 28. Bathias C, Paris PC. In: Faulkner L, ed. *Gigacycle Fatigue in Mechanical Practice*. New York: Marcel Dekker; 2005.
 29. Shamsaei N, Simsirowong J. Fatigue behaviour of additively-manufactured metallic parts. *Procedia Struct Integr.* 2017;7:3-10.
 30. Murakami Y, Yokoyama NN, Nagata J. Mechanism of fatigue failure in ultralong life regime. *Fatigue Fract Eng Mater Struct.* 2002;25(8-9):735-746.
 31. Murakami Y. *Metal Fatigue: Effects of Small Defects And Non-metallic Inclusions*. Elsevier; 2002.
 32. Tenkamp J, Awd M, Siddique S, Starke P, Walther F. Fracture-mechanical assessment of the effect of defects on the fatigue lifetime and limit in cast and additively manufactured aluminum-silicon alloys from HCF to VHCF regime. *Metals (Basel).* 2020;10:1-18.
 33. Siddique S, Imran M, Wycisk E, Emmelmann C, Walther F. Fatigue assessment of laser additive manufactured AlSi12 eutectic alloy in the very high cycle fatigue (VHCF) range up to 1E9 cycles. *Mater Today Proc.* 2016;3(9):2853-2860.
 34. Siddique S, Imran M, Walther F. Very high cycle fatigue and fatigue crack propagation behavior of selective laser melted AlSi12 alloy. *Int J Fatigue.* 2017;94:246-254.
 35. Siddique S, Awd M, Tenkamp J, Walther F. High and very high cycle fatigue failure mechanisms in selective laser melted aluminum alloys. *J Mater Res.* 2017;32(23):4296-4304.
 36. Awd M, Siddique S, Walther F. Microstructural damage and fracture mechanisms of selective laser melted Al-Si alloys under fatigue loading. *Theor Appl Fract Mech.* 2020;106:102483.
 37. Siddique S, Imran M, Wycisk E, Emmelmann C, Walther F. Influence of process-induced microstructure and imperfections on mechanical properties of AlSi12 processed by selective laser melting. *J Mater Process Technol.* 2015;221:205-213.
 38. Awd M, Siddique S, Johannsen J, Emmelmann C, Walther F. Very high-cycle fatigue properties and microstructural damage mechanisms of selective laser melted AlSi10Mg alloy. *Int J Fatigue.* 2019;124:55-69.
 39. Tridello A, Biffi CA, Fiocchi J, et al. VHCF response of as-built SLM AlSi10Mg specimens with large loaded volume. *Fatigue Fract Eng Mater Struct.* 2018;41(9):1918-1928.
 40. Tridello A, Fiocchi J, Biffi CA, et al. VHCF response of Gaussian SLM AlSi10Mg specimens: Effect of a stress relief heat treatment. *Int J Fatigue.* 2019;124:435-443.
 41. Tridello A, Fiocchi J, Biffi CA, et al. Influence of the annealing and defects on the VHCF behavior of an SLM AlSi10Mg alloy. *Fatigue Fract Eng Mater Struct.* 2019;42(12):2794-2807.
 42. Paolino DS, Tridello A, Fiocchi J, et al. VHCF response up to 109 cycles of SLM AlSi10Mg specimens built in a vertical direction. *Appl Sci.* 2019;9(15):1-13.
 43. Tridello A, Fiocchi J, Biffi CA, et al. Effect of microstructure, residual stresses and building orientation on the fatigue response up to 109 cycles of an SLM AlSi10Mg alloy. *Int J Fatigue.* 2020;137:105659.
 44. Tridello A, Fiocchi J, Biffi CA, et al. Size-effects affecting the fatigue response up to 10⁹ cycles (VHCF) of SLM AlSi10Mg specimens produced in horizontal and vertical directions. 1-28.
 45. Fiocchi J, Tuissi A, Bassani P, Biffi CA. Low temperature annealing dedicated to AlSi10Mg selective laser melting products. *J Alloys Compd.* 2017;695:3402-3409.
 46. Biffi CA, Fiocchi J, Bassani P, et al. Microstructure and preliminary fatigue analysis on AlSi10Mg samples manufactured by SLM. *Procedia Struct Integr.* 2017;7:50-57.
 47. Colombo C, Biffi CA, Fiocchi J, Tuissi A, Vergani LM. Effect of optimized heat treatments on the tensile behavior and residual stresses of selective laser melted AlSi10Mg samples. *Key Eng Mater.* 2019;813:364-369.
 48. Qian G, Jian Z, Qian Y, Pan X, Ma X, Hong Y. Very-high-cycle fatigue behavior of AlSi10Mg manufactured by selective laser melting: Effect of build orientation and mean stress. *Int J Fatigue.* 2020;138:105696.
 49. Jian ZM, Qian GA, Paolino DS, Tridello A, Berto F, Hong YS. Crack initiation behavior and fatigue performance up to very-high-cycle regime of AlSi10Mg fabricated by selective laser melting with two powder sizes. *Int J Fatigue.* 2021;143:106013.
 50. Lesperance X, Ilie P, Ince A. Very high cycle fatigue characterization of additively manufactured AlSi10Mg and AlSi7Mg aluminium alloys based on ultrasonic fatigue testing. *Fatigue Fract Eng Mater Struct.* 2020;1-9.
 51. Ilie P, Lesperance X, Ince A. Development of an ultrasonic fatigue testing system for gigacycle fatigue. *Mater Des Process Commun.* 2019;1-9.
 52. Wycisk E, Siddique S, Herzog D, Walther F, Emmelmann C. Fatigue performance of laser additive manufactured Ti-6Al-4V in very high cycle fatigue regime up to 10⁹ cycles. *Front Mater.* 2015;2:2-9.
 53. Günther J, Krewerth D, Lippmann T, et al. Fatigue life of additively manufactured Ti-6Al-4V in the very high cycle fatigue regime. *Int J Fatigue.* 2017;94:236-245.
 54. Heinz S, Balle F, Wagner G, Eifler D. Analysis of fatigue properties and failure mechanisms of Ti6Al4V in the very high cycle fatigue regime using ultrasonic technology and 3D laser scanning vibrometry. *Ultrasonics.* 2013;53(8):1433-1440.
 55. Tridello A, Fiocchi J, Biffi CA, et al. VHCF response of heat-treated SLM Ti6Al4V Gaussian specimens with large loaded volume. *Procedia Struct Integr.* 2019;18:314-321.
 56. Paolino DS, Tridello A, Chiandussi G, Rossetto M. On specimen design for size effect evaluation in ultrasonic gigacycle fatigue testing. *Fatigue Fract Eng Mater Struct.* 2014;37(5):570-579.
 57. Du L, Qian G, Zheng L, Hong Y. Influence of processing parameters of selective laser melting on high-cycle and very-high-cycle fatigue behaviour of Ti-6Al-4V. *Fatigue Fract Eng Mater Struct.* 2020;1-17.

58. Xu W, Sun S, Elambasseril J, Liu Q, Brandt M, Qian M. Ti-6Al-4V additively manufactured by selective laser melting with superior mechanical properties. *Jom*. 2015;67(3):668-673.
59. Liu J, Sun Q, Zhou C, et al. Achieving Ti6Al4V alloys with both high strength and ductility via selective laser melting. *Mater Sci Eng A*. 2019;766:138319.
60. Qian G, Li Y, Paolino DS, Tridello A, Berto F, Hong Y. Very-high-cycle fatigue behavior of Ti-6Al-4V manufactured by selective laser melting: Effect of build orientation. *Int J Fatigue*. 2020;136:105628.
61. Liu F, He C, Chen Y, Zhang H, Wang Q, Liu Y. Effects of defects on tensile and fatigue behaviors of selective laser melted titanium alloy in very high cycle regime. *Int J Fatigue*. 2020;140:105795.
62. Heinz S, Eifler D. Crack initiation mechanisms of Ti6Al4V in the very high cycle fatigue regime. *Int J Fatigue*. 2016;93:301-308.
63. Liu Z, Wang Z, Gao C, Liu R, Xiao Z. Microstructure, anisotropic mechanical properties and very high cycle fatigue behavior of Ti6Al4V produced by selective electron beam melting. *Met Mater Int*. 2020;1-12.
64. Yang K, Huang Q, Wang Q, Chen Q. Competing crack initiation behaviors of a laser additively manufactured nickel-based superalloy in high and very high cycle fatigue regimes. *Int J Fatigue*. 2020;136:105580.
65. Chen Q, Kawagoishi N, Wang QY, Yan N, Ono T, Hashiguchi G. Small crack behavior and fracture of nickel-based superalloy under ultrasonic fatigue. *Int J Fatigue*. 2005;27(10-12):1227-1232.
66. Muhammad M, Frye P, Simsiriwong J, Shao S, Shamsaei N. An investigation into the effects of cyclic strain rate on the high cycle and very high cycle fatigue behaviors of wrought and additively manufactured Inconel 718. *Int J Fatigue*. 2020;106038.
67. Li W, Sun R, Wang P, et al. Subsurface faceted cracking behavior of selective laser melting Ni-based superalloy under very high cycle fatigue. *Scr Mater*. 2021;194:113613.
68. Voloskov B, Evlashin S, Dagesyan S, Abaimov S, Akhatov I, Sergeichev I. Very high cycle fatigue behavior of additively manufactured 316L stainless steel. *Materials (Basel)*. 2020;13:1-11.
69. Spierings AB, Starr TL, Wegener K. Fatigue performance of additive manufactured metallic parts. *Rapid Prototyp J*. 2013;19(2):88-94.
70. Leuders S, Lienenke T, Lammers S, Tröster T, Niendorf T. On the fatigue properties of metals manufactured by selective laser melting—The role of ductility. *J Mater Res*. 2014;29(17):1911-1919.
71. Xiong Z, Naoe T, Futakawa M. Effect of artificial defects on the very high cycle fatigue behavior of 316L stainless steel. *Metals (Basel)*. 2019;9:1-11.

How to cite this article: Caivano R, Tridello A, Chiandussi G, Qian G, Paolino D, Berto F. Very high cycle fatigue (VHCF) response of additively manufactured materials: A review. *Fatigue Fract Eng Mater Struct*. 2021;1-25. doi:10.1111/ffe.13567